ARTICLE IN PRESS

Materials Science & Engineering C xxx (xxxx) xxx

Contents lists available at ScienceDirect

Materials Science & Engineering C

journal homepage: www.elsevier.com/locate/msec

The contracture-in-a-well. An in vitro model distinguishes bulk and interfacial processes of irreversible (fibrotic) cell-mediated contraction

Iwan Vaughan Roberts [a,1], Roberto Donno [b], Francesco Galli [c], Christopher Yusef Leon Valdivieso [a,2], Alessandro Siani [a,3], Giulio Cossu [c], Annalisa Tirella [a,4], Nicola Tirelli [a,b,*]

[a] *Division of Pharmacy and Optometry, School of Health Science, University of Manchester, Oxford Road, Manchester M13 9PT, United Kingdom*
[b] *Laboratory of Polymers and Biomaterials, Fondazione Istituto Italiano di Tecnologia, via Morego 30, 16163 Genova, Italy*
[c] *Division of Cell Matrix Biology & Regenerative Medicine, School of Biology, University of Manchester, Oxford Road, Manchester M13 9PT, United Kingdom*

ARTICLE INFO

Keywords:
Cell alignment
Cell-matrix interactions
Contraction
Contracture
Fibrin
Fibrosis
Myofibroblasts
Duchenne muscular dystrophy
Scarring

ABSTRACT

Tissue contractures are processes of cell-mediated contraction, irreversible in nature and typically associated with fibrotic phenomena. Contractures can be reproduced in vitro; here, we have used a medium-throughput model based on fibroblast-seeded fibrin (the ‘contracture well’). Firstly, we show how profoundly these processes depend on the location of the contractile cells: when on top of the material, fibroblasts produce an interfacial contracture (analog to capsular contraction around an implant), which tries and bends the construct; when seeded inside the material, they initiate a bulk contracture (analogue to a wound bed closure) that shrinks it from within. Secondly, we demonstrate that the interfacial and bulk contractures are also mechanically and biologically different processes. Thirdly, we show the potentially predictive value of this model, since it not only recapitulates the effect of pro-fibrotic factors (TGF-β1 for dermal (myo)fibroblasts), but can also indicate the fibrotic potential of a given cell population (here, dystrophic myoblasts more fibrotic than healthy or genetically corrected ones), which may have important implications in the identification of appropriate therapies.

1. Introduction

Cell-mediated contraction processes can be rapid and reversible, e.g. in the build-up of tension in muscles, or slower and irreversible, e.g. in scar formation. The latter are typically referred to as contractures and can fulfil beneficial (e.g. closure of a wound [1] or proper tissue morphogenesis [2]) or pathological roles (e.g. hypertrophic scarring [3], organ fibrosis [4], or capsule formation around implants [5]). The healthcare significance of contractures can be better understood by considering that virtually all large burns produce keloids and/or hypertrophic scarring, [6] or that the best known contracture-associated pathology - Dupuytren's disease - has a prevalence estimated between 1 and 30% of the adult Western population depending on the age group (increasing with age) [7]. Contractures can also be observed in in vitro systems: extracellular matrix (ECM) contracture and orientation by cells is instrumental to obtain tendon/ligament-[8,9], muscle-[10] or peripheral nerve[11]-mimicking constructs. Of note, ECM contracture can reduce cell viability, e.g. for chondrocytes [12–14].

Here, we have mechanistically studied in vitro contracture, in order to quantitatively assess the effect of design/(micro)environmental parameters (nature of the ECM, mechanical constraints, cell location, pro-fibrotic factors), and eventually generate predictive fibrotic models,

---

Abbreviations: TGF-β1, Transforming Growth Factor Beta 1; HDFa, Human Dermal Fibroblasts (adult); α-SMA, Alpha Smooth Muscle Actin; ECM, Extracellular Matrix; SEM, Scanning Electron Microscopy; PDMS, Polydimethylsiloxane.

[*] Corresponding author at: Laboratory of Polymers and Biomaterials, Fondazione Istituto Italiano di Tecnologia, via Morego 30, 16163 Genova, Italy.
E-mail address: nicola.tirelli@iit.it (N. Tirelli).

[1] Current address: Department of Clinical Neuroscience, University of Cambridge, Cambridge Biomedical Campus, Cambridge, CB2 0AH, United Kingdom

[2] Current address: Department of Polymers for Health and Biomaterials, Max Mousseron Institute of Biomolecules (IBMM), UMR CNRS 5247, University of Montpellier, France

[3] Current address: School of Biological Sciences, University of Portsmouth, King Henry Building, King Henry 1st Street, Portsmouth PO1 2DY, United Kingdom.

[4] Current address: BIOtech - Center for Biomedical Technologies, Department of Industrial Engineering, University of Trento, Via delle Regole 101, Trento 38123, Italy.

https://doi.org/10.1016/j.msec.2022.112661
Received 14 November 2021; Received in revised form 4 January 2022; Accepted 7 January 2022
Available online 13 January 2022

0928-4931/© 2022 The Authors. Published by Elsevier B.V. This is an open access article under the CC BY-NC-ND license (http://creativecommons.org/licenses/by-nc-nd/4.0/).

Please cite this article as: Iwan Vaughan Roberts, *Materials Science & Engineering C*, https://doi.org/10.1016/j.msec.2022.112661

using adult human dermal fibroblasts (HDFa) as a cellular model in most of the study.

1.1. Fibrin is a contractible ECM

Fibrin is a popular injectable matrix, which is capable to host cells and be remodeled by them into a variety of functional tissues [15]; it is widely applied in the clinic as a sealant [16], and has widespread laboratory use as an artificial ECM [17]. As the natural provisional matrix laid down during wound healing, fibrin and its remodelling plays a key role in tissue contracture and scarring. Indeed fibrin is naturally contracted by cells; for example, platelet-mediated compaction of fibrin networks is crucial to reduce the size of blood clots. [18–20] Here, we have produced gels using fibrinogen at a concentration of 3.125, 6.25 and 12.5 mg/mL (Fig. 1A), a range similar to that in human blood (2–5 mg/mL [19]). The moduli of the resulting gels (Fig. 1A, bottom) are close to those of several soft tissues (0.1–10 kPa dermis [21]; 0.7–6 kPa lungs [22]; 12 kPa skeletal muscles [23,24]; 0.5–3/10–15 kPa for healthy/fibrotic liver, 1.5/2 kPa for white brain white/grey matter [25]); this makes fibrin suitable for modelling cell-mediated contracture of similarly soft tissues.

1.2. Axial anchoring is a beneficial form of mechanical constraint

Contraction of cell-laden matrices is often evaluated on freely floating constructs. [26–29] These models are far from ideal: firstly, they do not model physiological processes, where mechanical anchoring to surrounding tissues is the norm. Secondly, uncontrolled contracture is often detrimental to the viability of embedded cells (see Supporting Information, Fig. 3SI, 4SI, 6SI). Indeed, several approaches have been explored to reduce fibrin unconstrained and thus uncontrolled contraction, e.g. by mixing it with components that e.g. osmotically counter contracture (e.g. hyaluronic acid[30] or poly(ethylene glycol) (PEG) [31]), or are sufficiently hard to mechanically resist to it. [14,32] Thirdly, anchored and non-anchored models contract differently: confluent layers of fibroblasts can assemble in tendon-like structures only when pins anchor them axially [33]. A directional constraint (axial anchoring) offers both simplicity and efficacy.

1.3. 3D vs. 2D cell positioning

Key to this study is the comparison of two contracture modes, which differ in where cells are seeded, i.e. on top of fibrin or within it (Fig. 1C), here respectively referred to as 2D- and 3D-seeding. 2D-seeding should lead to constructs folding without significant volumetric changes (‘wrapping'); this provides a model of interfacial, 2D fibrosis, similar to capsular contraction around non-degradable foreign bodies (e.g. silicone implants). 3D-seeding should determine a bulk contracture (‘shrinkage’) that more closely resembles scar formation. Of note, we have previously shown that HDFa migration rate within fibrin, and the mechanical properties of the latter, are insensitive to protease inhibitors [34] for at least one week, which suggests insignificant matrix remodelling by 3D-seeded HDFa in the time frame of the experiments of this study, which is indeed at most one week.

The two models, therefore, mimic fibrotic/contracture processes that are both geometrically and physiologically different, and thus in perspective may allow for a targeted assessment of the efficacy of anti-fibrotic therapies.

1.4. The contracture well

Fibroblast-loaded fibrin has been used to produce tendons [35] and - with calcium phosphate anchors - ligaments [9,36], through processes of in vitro contractures. One of the novel points of this study is the introduction of a medium-throughput approach, where each well of 12-well plate is a complete contracture unit (the ‘contracture well’). Such a system allows for a quantitative comparison of the fibrotic potential of physical, cellular or molecular variables, thereby also possibly permitting predictions of the fibrotic or anti-fibrotic effects of specific conditions. In this regard, a number of factors are known to promote myofibroblastic differentiation of fibroblasts and increase their contractility, which can be used to validate the model and show its predictive potential; here we have employed possibly the best known among these factors, the transforming growth factor beta (TGF-β1) [37,38].

2. Results and discussion

2.1. Optimization of the contracture well model

2.1.1. Cell density in 3D

In view of a reproducible performance of a cell-laden construct, cell density is a critical parameter. We have tackled its optimization using HDFa as a model with the aims a) to maximize viability and proliferation, and b) to allow the contracture process to last a few days, which is a typical duration for the closure of a wound bed. Typical values of cell density in 3D-seeded constructs vary from 2×10^5 cells/mL [28,39] to $1–3 \times 10^6$ cells/mL [40,41], and we have therefore focused on finding an optimal value within this range.

The proportion of dead cells increased with increasing cell numbers (Fig. 2A). The threshold for significant cell death (around 1 M cells/mL) is relatively low, and is likely caused by the hypoxia/necrosis during contraction of these rather thick (around 1 mm) constructs.

However, at the lowest density (2×10^5 cells/mL) 3D-seeded HDFa retained both viability and proliferative activity (in Supporting Information, see Fig. 3SI, panel B, Fig. 4SI, panel B, and Fig. 5SI); as a testimony of the cell health at this density, resazurin fluorescence grew with time, in a fashion qualitatively similar to what observed on plastics (Fig. 2B). Since low densities also allowed for more gradual contraction kinetics (Fig. 2C), we adopted 2×10^5 cells/mL as the volumetric cell density for all further 3D experiments. Of note, lower densities did not allow the contracture process to stabilize within one week and were not further analyzed.

2.2. Cell density in 2D

HDFa were seeded at 5000 cells/cm^2, which provided both high viability and proliferation activity (see Supporting Information, Fig. 3SI, panel C, and Fig. 4SI, panel C). This density roughly corresponds to an initial 30% surface coverage (assuming an area of min. 5000 μm^2/cell, as measured on neonatal HDF [42]); resazurin fluorescence increases steadily with time, likely reaching confluence by day 4, and suggesting that at later time points HDFa may have formed multilayers.

2.3. Anchoring or not

Since fibrin gels do not directly adhere to the underlying Pluronic-treated silicone, their anchoring points determine the contracture geometry and therefore can affect the extent of shrinkage, and in turn influence the activity and survival of embedded cells. Indeed, 3D-seeded cells can only marginally proliferate in case of unconstrained contracture (freely floating, non-anchored constructs), as shown in Supporting Information (Fig. 3SI, panel A and Fig. 4SI, panel A). It is noteworthy that experiments were conducted with/without TGF-β1, which can promote contracture by inducing a myofibroblastic differentiation in HDFa [43], but is also a known anti-mitogenic factor. [44] In these freely floating matrices, HDFa proliferated only at the highest fibrin concentration and without TGF-β1 (see Supporting Information, Fig. 3SI, panel A and Fig. 4SI, panel A), i.e. in the only system that experienced a limited contracture (see Supporting Information, Fig. 6SI). In short, anchoring is beneficial not only for a guided contracture but also to avoid the detrimental effects on viability seen

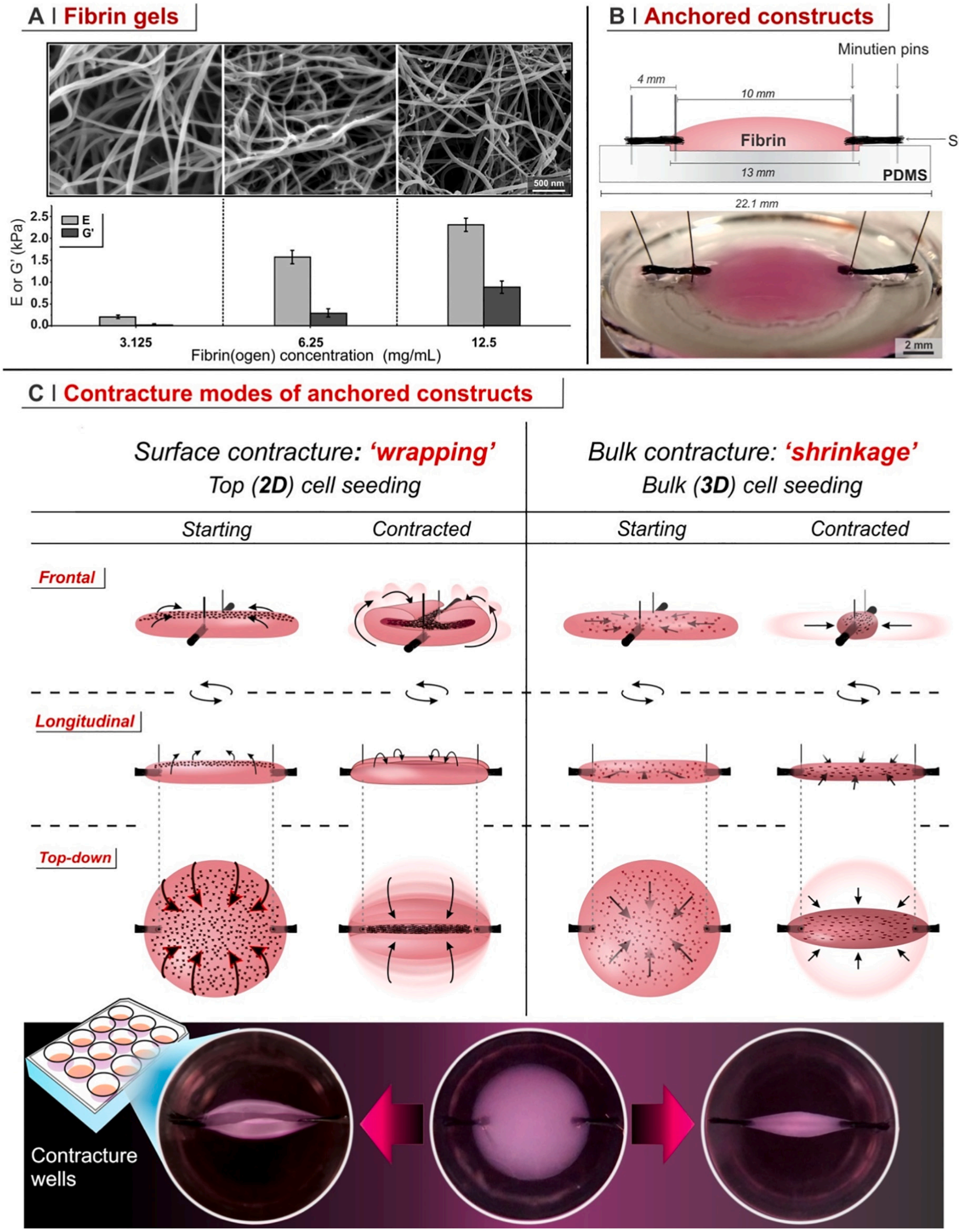
A | Fibrin gels
500 nm
E
G'
E or G' (kPa)
2.5
2.0
1.5
1.0
0.5
0.0
3.125
6.25
12.5
Fibrin(ogen) concentration (mg/mL)
B | Anchored constructs
Minutien pins
4 mm
10 mm
Fibrin
Suture
13 mm
PDMS
22.1 mm
2 mm
C | Contracture modes of anchored constructs
Surface contracture: 'wrapping'
Top (2D) cell seeding
Bulk contracture: 'shrinkage'
Bulk (3D) cell seeding
Starting
Contracted
Starting
Contracted
Frontal
Longitudinal
Top-down
Contracture wells

Fig. 1. *A.* Scanning Electron Microscopy (SEM) images (*top*), Young's modulus (E; in compression, strain 10%; *bottom*) and storage shear modulus (G') of gels obtained from 3.125, 6.25 and 12.5 mg/mL fibrinogen; $n = 3$. SEM images show the difference in fibre density, which may be the main determinant of the slower HDFa migration through more concentrated gels [34]. Gels are identified in reference to the initial fibrinogen concentration; the fibrin concentration in the gels is more complex, due to their different swelling in culture media. *B.* Scheme (*top*) and image (*bottom*) of an anchored fibrin gel. Sutures secure the gels to pins inserted in an indented PDMS layer (see its cross-section in Supporting Information, Fig. 1SI). *C.* The contracture geometry depends on where cells are seeded. Substrates are seen along the anchor axis (*transverse*), perpendicular to it (*longitudinal*), or from above (*top-down*); arrows indicate directions of contracture. With 2D-seeded cells (*surface - left*), the material 'wraps' around an axis, eventually resembling a hollow tube. With cells dispersed within the construct (*bulk – right*), the material shrinks around the anchor axis. The pictures at the bottom show the two types of contracture in wells of a 12-well plate.

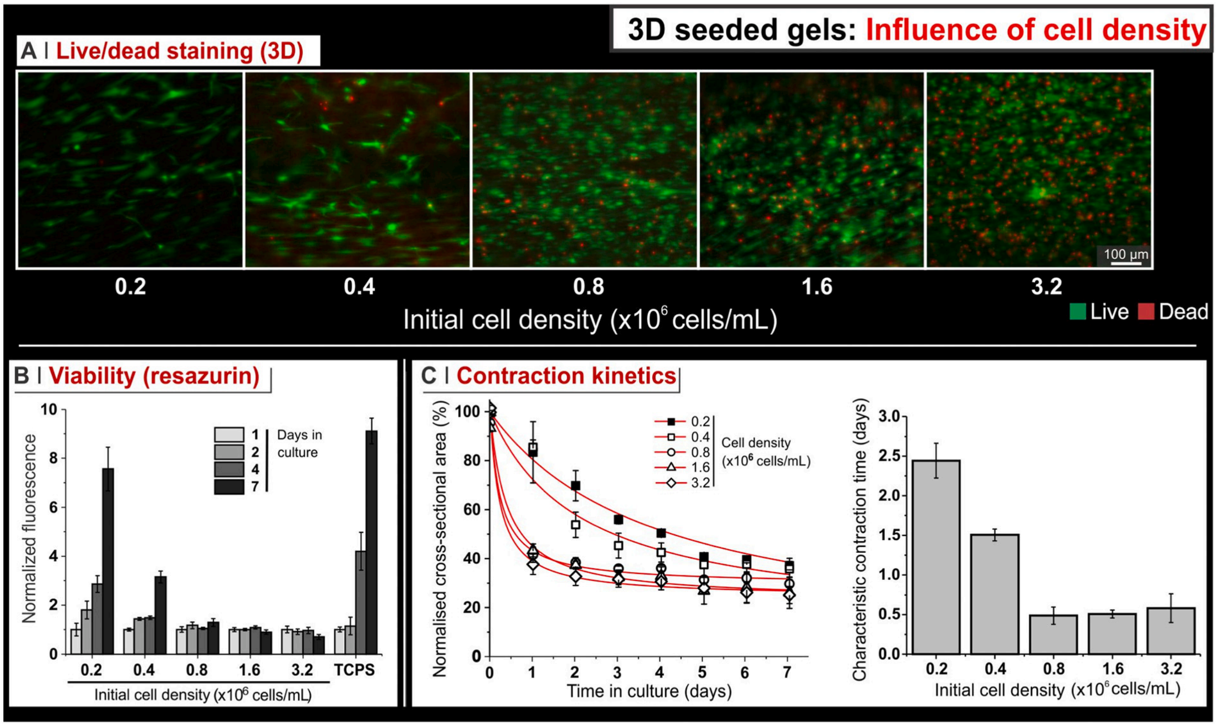

Fig. 2. *A.* At day 7, live cells were stained by Calcein-AM (green), and the nuclei of dead cells by propidium iodide (red) in 6.25 mg/mL 3D-seeded and axially anchored gels. *B.* Cell metabolic activity was measured via the resazurin metabolic assay (Alamar Blue assay, see Supporting Information, Fig. 2SI)) at days 1, 2, 4 and 7 of culture. Values are normalized to the day 1 fluorescence. *C.* The time-dependent normalized cross-sectional area of constructs 3D-seeded with different cell densities (*left*) can be fitted with a Boltzmann model (red lines); the centroid of the corresponding curves is taken as the characteristic contracture time (*right*). $n = 6$. (For interpretation of the references to colour in this figure legend, the reader is referred to the web version of this article.)

with the rapid and unconstrained contracture observed in freely floating gels.

2.4. *Kinetic similarities in fibroblast-mediated 2D and 3D contracture*

In the contracture well model, constructs evolve from a circular to an elongated shape (Fig. 3A and C); this can be followed using aspect ratio or cross-sectional area as quantitative descriptors. The two parameters provide essentially the same geometrical information, and indeed are inversely related (see Supporting Information, Fig. 7SI and 8SI); however, cross-sectional area data have generally a lower variability, and are therefore better candidates to characterize the contracture kinetics (see Supporting Information, the red sigmoidal lines in Fig. 6SI, panel B, and Fig. 8SI, panels A and C, are Boltzmann fittings) with numerical parameters; in the latter role, we have employed the final cross-sectional area and the characteristic time, in order to separately account for the contractile capacity of the cell population, and for the speed of the contracture, respectively.

The key results of this analysis apply to both the 'shrinking' (3D) and 'wrapping' (2D) contracture, and indicate that:

a) stiffer substrates were contracted less and more slowly (Fig. 3B and D for 3D; Fig. 3F and H for 2D); as a limit case, without TGF-β1 12.5 mg/mL fibrin (Young's modulus ~2.3 kPa) was hardly contracted in both geometries.
b) TGF-β1 increased the contractile capacity but did not have a clear influence on the speed: no difference for 3.125 mg/mL fibrin(ogen) constructs, and contradicting effects for the others (compare white and black symbols in Fig.s 3B and 3D for 3D constructs, Fig.s 3F and 3G for 2D ones).
c) when cells are capable to exert significant contracture, speed and capacity of contraction appeared to be related, i.e. the more a matrix can be contracted, the quicker it will be contracted (Fig. 3I).

It is noteworthy that 2D and 3D contractures are kinetically similar: the fastest and the slowest systems in shrinkage are also respectively the fastest and slowest in wrapping (Fig. 3J and K).

Of note, freely floating gels did not show any meaningful correlation between both the extent or the speed of their unconstrained contracture and the construct stiffness (see Supporting Information, Fig. 3SI, panel C).

2.5. *Myofibroblastic character enhances, but is not crucial for contracture*

Myofibroblastic phenotypes are most often identified as α-smooth muscle actin (α-SMA)-positive cells and are encountered in most fibrotic contractures. Despite a heterogeneous origin and an intrinsic phenotypic plasticity [43], there are two minimal denominators: a) fibroblasts (and protomyofibroblasts [45]) develop into fully differentiated myofibroblasts under the influence of TGF-β1 [46,47] or other pro-fibrotic factors such as platelet-derived growth factor (PDGF)[48,49]; b) myofibroblasts differ from (quiescent) fibroblasts for an enhanced contractile character, presence α-SMA-positive stress fibres and enhanced collagen type I production. [50] Of note, also ED-A fibronectin can be used as a marker, but is less selective than α-SMA: firstly, it is an early marker, which then persists during full differentiation; for example, it is typically already recorded in HDFa cultured on plastic in the absence of fibrotic factors. Secondly, its detection may strongly depend on its fibrillation state. [45].

2.5.1. *α-SMA*

In our models, α-SMA-positive cells were detected only upon TGF-β1 treatment, both in 3D (Fig. 4A, left) and 2D contracture (Fig. 4B, left). α-SMA mRNA expression broadly confirmed this (see Supporting Information, Fig. 9SI, panels A and B); for example, α-SMA was barely detectable in untreated 2D-seeded constructs, and TGF-β1 treatment elevated its levels only to approach those of untreated HDFa on plastics.

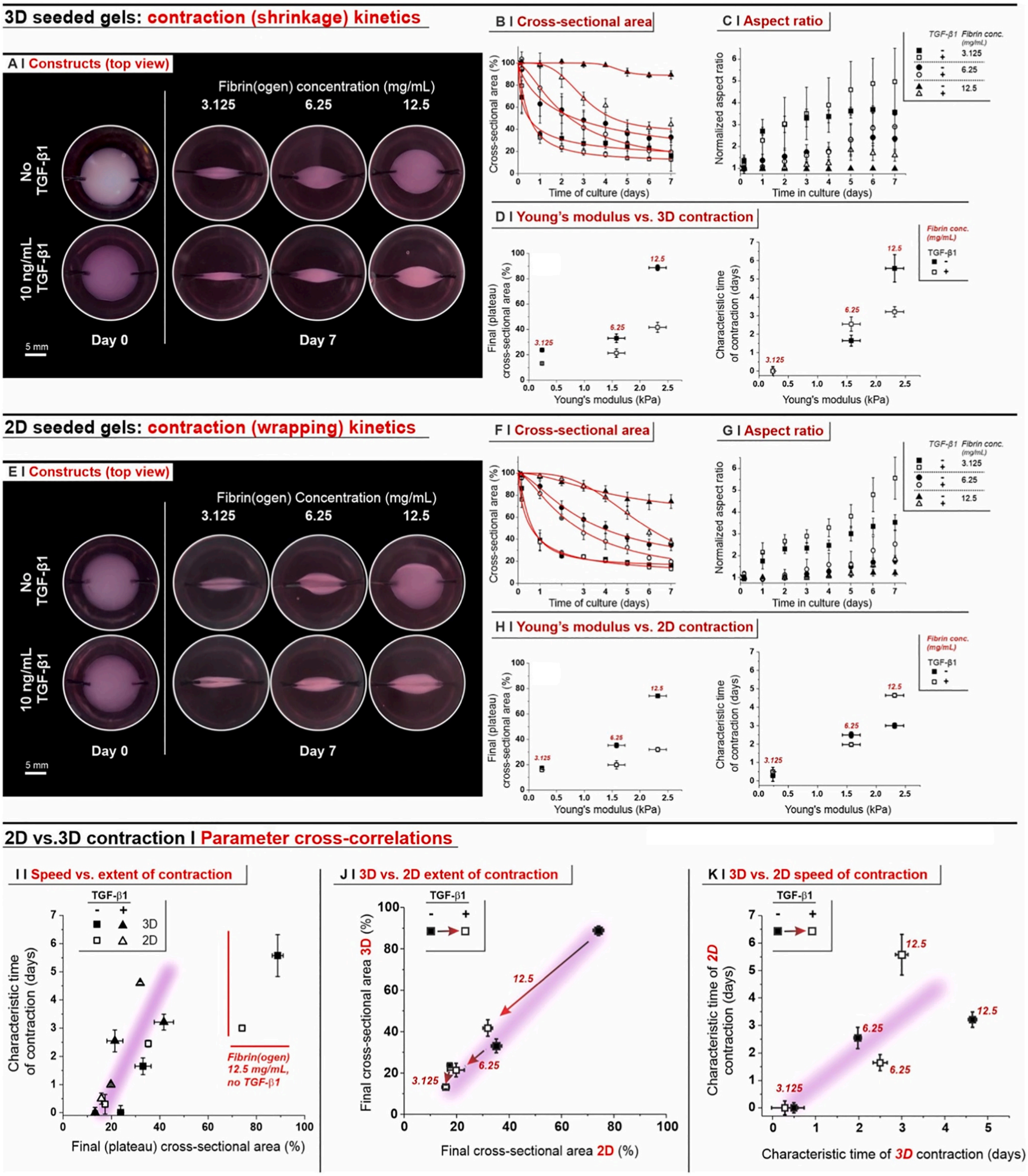

Fig. 3. *A.* Views from above of the contracture (shrinkage) of 3D-seeded, axially anchored constructs as a function of fibrin initial concentration and presence of TGF-β1. The sutures anchoring the constructs to the metallic pins are visible as dark lines at the two ends of the horizontal axis. *B-C.* The final cross-sectional area (*panel B*) and the characteristic time (*panel C*) are numerical parameters extracted from the time dependency of the cross-sectional area (see Supporting Information, Fig.s 6SI and 8SI). *D.* Both parameters scale with the initial hardness of the material. *E-H.* Same as in panels A to E, but for 2D-seeded constructs. A time-lapse of the contracture processes is available in the Supporting Information; a first movie presents the phenomenon at the level of whole wells (Contracture_wells_Roberts.mp4), while a second in a magnified fashion at the level of suture ponts (Contracture_magnified_Roberts.mp4). *I-K.* In all samples undergoing significant contracture (i.e. all samples but 12.5 mg/mL fibrin gels without TGF-β1) speed and final extent of contraction correlate well (*panel I*); the blurred purple line is just a guide for the eyes. There is also a remarkable correlation among the final cross-sectional areas in the two contraction geometries (*panel J*), with remarkably similar effects of the TGF-β1treatment (arrows). A similar 2D/3D correlation can also be seen also for the speed of contraction (*panel K*); the somehow weaker correlation may stem from the higher variability in this parameter seen in samples undergoing hardly any contracture. For all panels, $n = 6$. (For interpretation of the references to colour in this figure legend, the reader is referred to the web version of this article.)

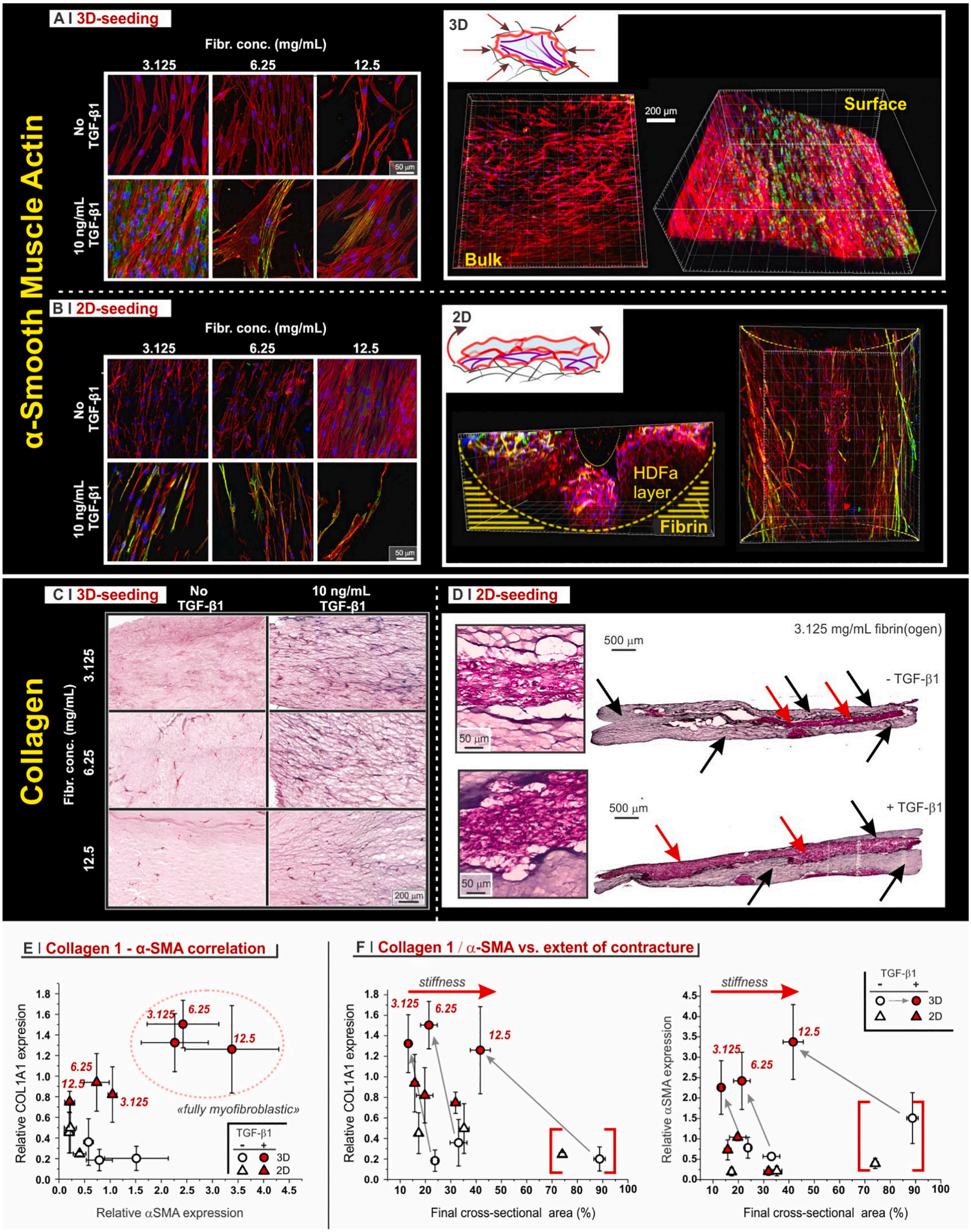
α-Smooth Muscle Actin
A | 3D-seeding
Fibr. conc. (mg/mL)
3.125
6.25
12.5
No TGF-β1
10 ng/mL TGF-β1
50 µm
3D
200 µm
Surface
Bulk
B | 2D-seeding
Fibr. conc. (mg/mL)
3.125
6.25
12.5
No TGF-β1
10 ng/mL TGF-β1
50 µm
2D
HDFa layer
Fibrin
Collagen
C | 3D-seeding
No TGF-β1
10 ng/mL TGF-β1
Fibr. conc. (mg/mL)
3.125
6.25
12.5
200 µm
D | 2D-seeding
3.125 mg/mL fibrin(ogen)
500 µm
- TGF-β1
50 µm
500 µm
+ TGF-β1
50 µm
E | Collagen 1 - α-SMA correlation
Relative COL1A1 expresion
Relative αSMA expression
3.125
6.25
12.5
6.25
12.5
3.125
«fully myofibroblastic»
TGF-β1
-
+
3D
2D
F | Collagen 1 / α-SMA vs. extent of contracture
stiffness
3.125
6.25
12.5
Relative COL1A1 expresion
Final cross-sectional area (%)
stiffness
3.125
6.25
12.5
Relative αSMA expression
Final cross-sectional area (%)
TGF-β1
-
+
3D
2D

(caption on next page)

Fig. 4. *A-B. Left:* immunofluorescence of α-SMA (Green: α-SMA. Red: actin. Blue: nuclei) for 3D (*A*) and 2D (*B*)-seeded constructs (day 7), cryosectioned prior to staining. *Right:* 3D-seeded constructs develop a higher density of actin close to the surface (3D-rendered images of 3 mg/mL fibrin, TGF-β1, day 7); in 2D-seeded constructs fibrin is marked with yellow lines because HDFa did not invade it. *C.* Picrosirius Red staining (collagen I and III) of cryosectioned 3D-seeded constructs, day 7 days. The darker colour with TGF-β1 shows an increased presence of collagen. *D.* At day 7, prior to Picrosirius Red staining, the 2D-seeded constructs were cryosectioned orthogonally to their axis. Their shape was heavily distorted, but the presence of a collagen-rich (red arrows) area sandwiched between collagen-poor regions (black arrows) is apparent. *E.* The correlation between collagen 1 and α-SMA expression (see Supporting Information, Fig. 8SI) shows that only 3D-seeded and TGF-β1 treated constructs yield 'myofibroblastic' cells. $n = 6$. *F.* Correlation between collagen 1 (*left*) and α-SMA expression (right), and final cross-sectional area (the higher the area, the lower the contracture). Negligibly contracted samples (12.5 mg/mL fibrin, no TGF-β1) are highlighted in red brackets, and should be considered outliers. Grey arrows show the effect of TGF-β1 on 3D-seeded constructs; 2D-seeded constructs exhibit a similar reduction in areas, but allow or negligible development of myofibroblast markers. $n = 6$. (For interpretation of the references to colour in this figure legend, the reader is referred to the web version of this article.)

It is worth pointing out that both in 3D and 2D-seeded constructs the initial modulus had hardly any relevant effect on α-SMA production (see Supporting Information, Fig. 9SI, panels A and B).

In terms of localization, in 2D-seeded constructs α-SMA-positive cells were predominantly seen close to their folding edges (Fig. 4B, right), which may reflect the higher mechanical stresses acting on the edges of the materials; in 3D-seeded constructs, they were only seen on their surface (Fig. 4A, right), where cell density may also be higher (see Supporting Information, Fig. 5SI; note also the apparently higher density of actin fibres on the surface; Fig. 4A, right).

2.5.2. Collagen

In 3D-seeded constructs Picrosirius Red stain revealed a relatively homogeneous collagen distribution, with often a slight accumulation at the surface; this may be connected to the higher cell density mentioned above (Fig. 4C). The stain was more intense upon TGF-β1 treatment, which also tallies with collagen I RT-qPCR data (see Supporting Information, Fig. 8SI, panel C). A similar, TGF-β1 stimulated collagen production can also be seen in 2D-seeded constructs (see Supporting Information, Fig. 9SI, panel D). In the latter constructs, however, the collagen-rich areas are found in the fibroblast layer, i.e. on top of and not within fibrin; it may be hypothesized that the interfacial contracture is due to the cell-mediated contraction of the matrix of this layer. Neither Picrosirius stain nor mRNA analysis indicated an effect of the matrix modulus on collagen production in any of the constructs.

2.5.3. Contractile cell 'fingerprinting'

By cross-correlating α-SMA and collagen I production (PCR data), a phenotype with both markers upregulated, i.e. 'fully myofibroblastic', develops only in 3D-seeded constructs and under the action of TGF-β1 (Fig. 4E); the equally treated 2D-seeded systems only showed a mild increase in collagen. Interestingly, the extent of this differentiation did not appear to correlate to stiffness nor to degree of contracture (Fig. 4F).

A myofibroblastic phenotype, therefore, does not appear to be necessary for such constructs to undergo contracture, or to respond to a pro-fibrotic agent: TGF-β1 induced a similar increase in contracture in 2D and 3D-seeded constructs, despite the cells in the constructs showing a rather different 'myofibroblastic' character.

2.6. Contractures as isotonic (2D) or partially isometric (3D) affine processes

In the contracture well model, the application of axial constraints leads the cell-laden constructs to assume a macroscopically anisotropic shape; microscopically, this corresponds to a preferential orientation of ECM fibres (see Supporting Information, Fig. 10SI). When a macroscopic deformation of a material translates uniformly at any level of scale, e.g. with the same direction of alignment, that deformation is typically described as affine. Indeed, the affine approach is often used to rationalize the behaviour of ECM fibrillar components such as collagen, [51,52]. In our model, cells are an integral part of the anisotropic contraction, directly pulling ECM fibres (Fig. 5A); it is of interest whether the affine scheme applies not only to fibrin fibres but also to cell bodies, since the relevant literature provides evidence of this [53] but also of the contrary [52]. Indeed, HDFa bodies aligned to a high extent along the contraction axis (Fig. 5B and C, left panels). We have employed cytoskeletal stress fibres to quantify cell alignment, expressing it through an order parameter (see Section 2.3.3; in Supporting Information, examples of stress fibre angular distributions are reported in Fig. 11SI, panels D-G, while Fig. 12SI and 13SI provide the order parameter data). In 3D-seeded constructs, HDFa alignment depended on the initial elastic modulus and on the extent of contracture (Fig. 5A, right): the softest and more contractible matrices provided the highest alignment. In 2D-seeded constructs, HDFa did not invade the matrix (despite the absence of fibrinolysis inhibitors), but produced a cell- and collagen-rich layer on its top (Fig. 4D); there, they were highly aligned, independent of stiffness and contracture (Fig. 5B, right).

In the most studied contractile tissues – skeletal muscles - contractions are often classified as isometric (distances unchanged, pulling force increases) or isotonic (distances reduced, pulling force constant). If we assume internal tension (the 'tone') to be roughly proportional to cell alignment, 2D contracture would resemble an isotonic process: cell alignment is constant during contraction of the cell layer. In the contracture of 3D-seeded constructs, the distance between anchoring points is fixed, while the cell alignment is variable (stiffness-dependent); at least in its central parts, the process is therefore mostly isometric. Interestingly, on the surface of the 3D-contracted constructs, the matrix turned out to be essentially isotropic, while HDFa aligned their spindle-shaped bodies in the direction of the anchoring points (Fig. 5C); we interpret this as the affine deformation being overcome by matrix (but not cell) shrinkage in the peripheral areas. We are therefore inclined to consider the contracture of 3D-seeded constructs to be isometric when dominated by a geometric constraint, anisometric (possibly more isotonic) elsewhere.

2.7. Mechanical effects of 3D contracture

The contracture of 2D-seeded constructs does not alter the mechanical properties of fibrin: the process is not accompanied by any significant volume change or remodelling of these matrices. Conversely, we recorded a significant variation of stiffness in the contracture of 3D-seeded constructs, both using tensile tests (bulk) and nanoindentation (surface), due to the bulk/surface differences discussed above.

2.8. Tensile measurements (Fig. 6A)

First, it must be noted that the mere presence of HDFa had a minor effect on the stiffness of constructs, with a moderate hardening only of the softest ones (see Supporting Information, Fig. 16SI). Cell-mediated contracture, on the contrary, was always accompanied by significant stiffening (Fig. 6B-C), above all in the presence of TGF-β1; this effect was so noticeable that the softest constructs underwent the highest degree of stiffening (Fig. 6C) and as a result became the hardest (Fig. 6B).

Contracture may also have a (small) effect on stress relaxation; by using a double exponential model (inset in Fig. 6A, bottom), it is possible to separately account for a predominantly elastic / poroelastic ('instantaneous' relaxation, τ_1) and for a viscoelastic response ('delayed' relaxation, τ_2). $\tau_2$was unaffected by the presence of cells (at day 0) or by

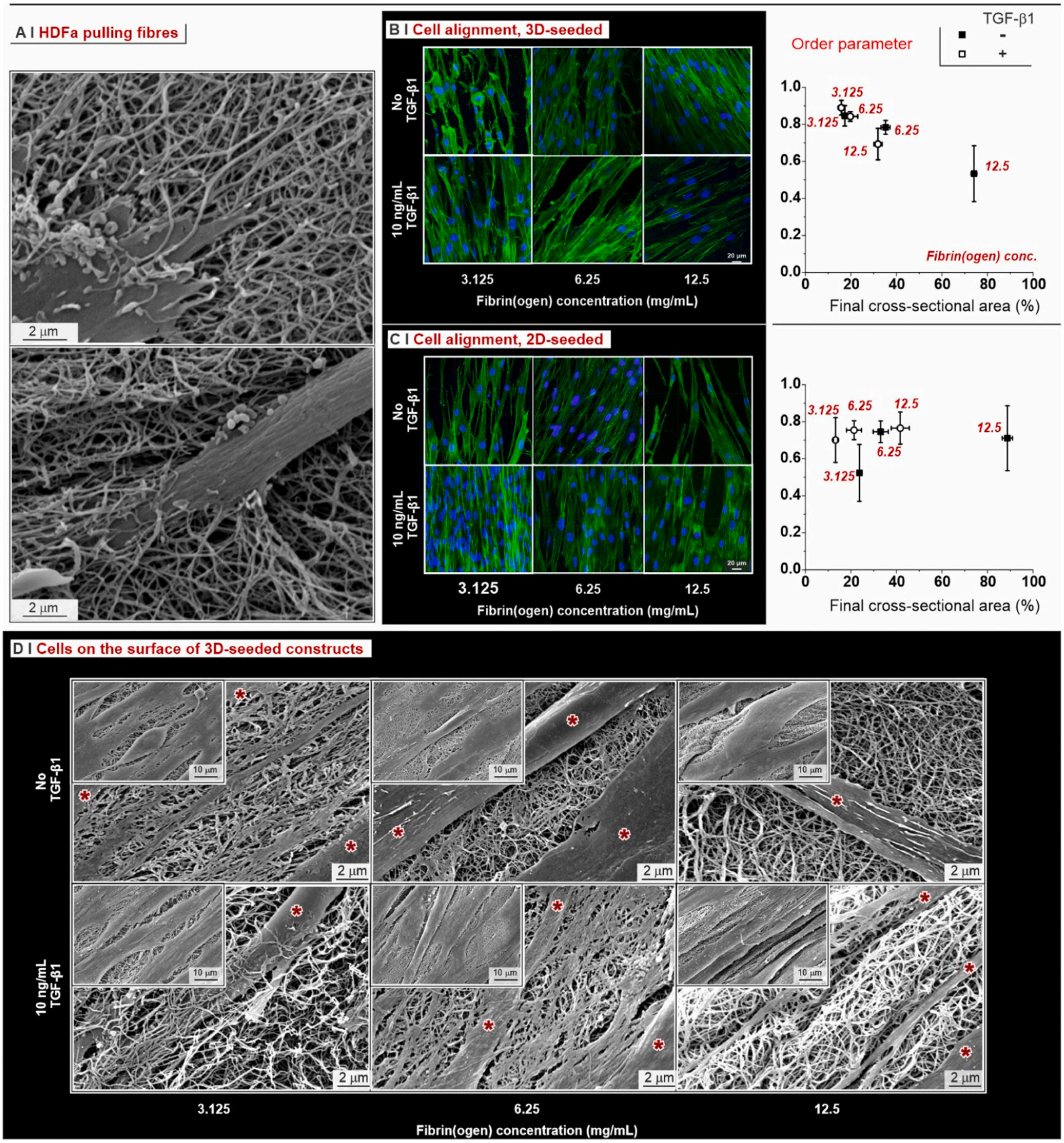
A I HDFa pulling fibres
2 μm
2 μm
B I Cell alignment, 3D-seeded
No TGF-β1
10 ng/mL TGF-β1
20 μm
3.125
6.25
12.5
Fibrin(ogen) concentration (mg/mL)
Order parameter
TGF-β1
■ -
□ +
1.0
0.8
0.6
0.4
0.2
0.0
0
20
40
60
80
100
Final cross-sectional area (%)
3.125
3.125
6.25
6.25
12.5
12.5
Fibrin(ogen) conc.
C I Cell alignment, 2D-seeded
No TGF-β1
10 ng/mL TGF-β1
20 μm
3.125
6.25
12.5
Fibrin(ogen) concentration (mg/mL)
3.125
6.25
12.5
12.5
6.25
3.125
Final cross-sectional area (%)
D I Cells on the surface of 3D-seeded constructs
No TGF-β1
10 ng/mL TGF-β1
10 μm
2 μm
3.125
6.25
12.5
Fibrin(ogen) concentration (mg/mL)

Fig. 5. *A.* SEM images of freeze-fractured 3D-seeded fibrin constructs (day 7), showing ECM fibres being 'pulled' by HDFa. *B. Left.* Confocal microscopy images of 3D-seeded constructs stained with phalloidin (green) and DAPI (blue). Of note, phalloidin provides a better signal-to-noise ratio than the anti-α-SMA antibody, which appears to stain also intermediate filaments (see also Supporting Information, Fig. 11SI, panel A to C), as also reported in literature. [54] *Right.* Correlation between cell alignment (order parameter S: 1 means perfect alignment, 0 random distribution; see also Supporting Information, Fig. 12SI) and extent of contracture; the order parameter data are also in Supporting Information, Fig. 13SI, panel A. *C.* As in panel *A*, but for 2D-seeded cells; the order parameter data are also in Supporting Information, Fig. 13SI, panel B. *D.* SEM images of 3D-seeded construct surfaces (day 7); in the pictures at higher magnification cellular processes are marked with a red star. Cells but not fibres show a preferential orientation. The high number of cells on the construct surfaces can also be seen by staining the constructs (see Supporting Information, Fig. 14SI). (For interpretation of the references to colour in this figure legend, the reader is referred to the web version of this article.)

contracture (day 7, with or w/o TGF-β1). τ_1, on the contrary appeared to be affected by contracture; before shrinkage, the softest samples showed higher τ_1 values, but after contracture no difference between samples could be noticed (Fig. 6D). This is a further indication that in a contracted state - and basically independent of its extent – all constructs were mechanically similar; a modulus in the range of 2–2.5 kPa may therefore be a self-limiting factor for HDFa-mediated matrix contracture. Finally, it is worth mentioning that no sample exhibited a statistically relevant difference in their strength, before or after contracture (Fig. 6E).

2.9. Nanoindentation

Firstly, this analysis showed that the construct surfaces became more mechanically heterogeneous after contracture (see Supporting Information, Fig. 11SI), above all with TGF-β1. This is likely due to cells migrating to the surface (Fig. 5D), where they are mechanically different from the surrounding matrix. The average surface elastic modulus

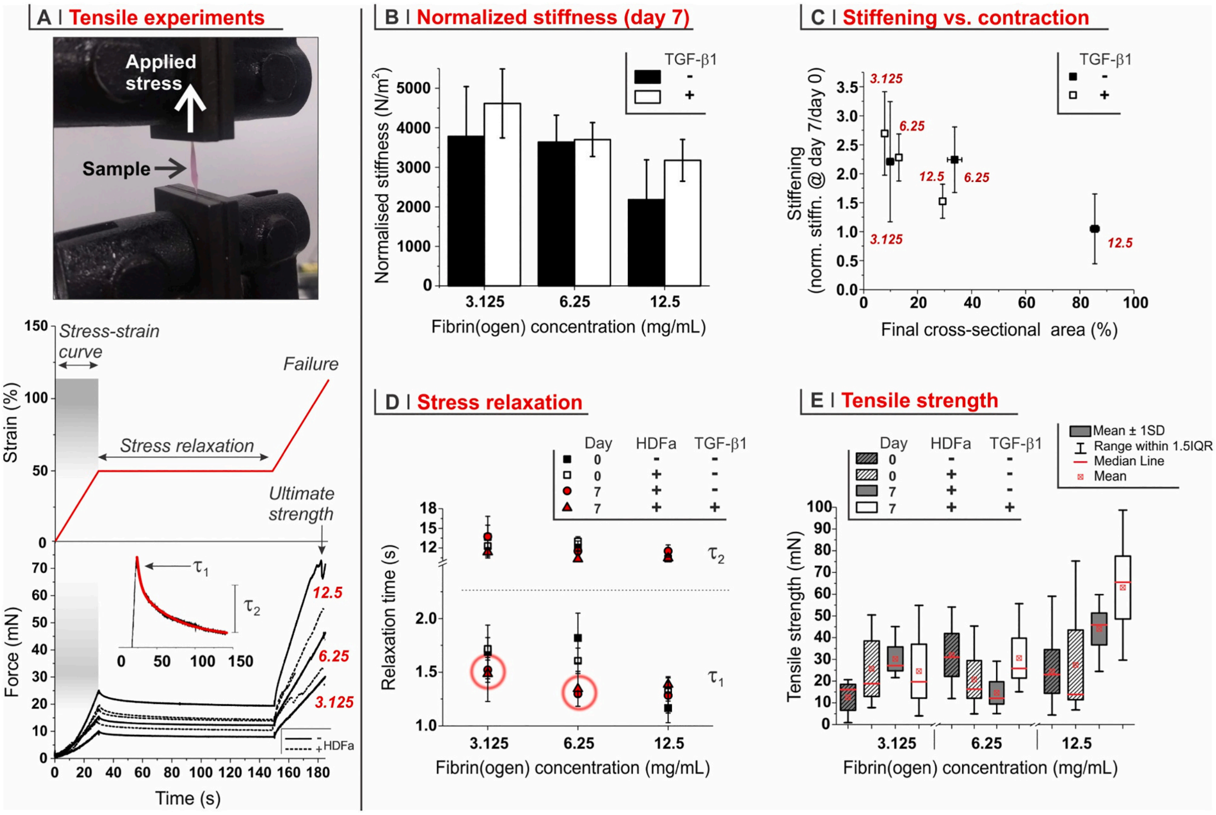

Fig. 6. *A.* 3D-seeded constructs were analyzed in tensile mode (see also Supporting Information, Fig. 15SI). A stress-strain curve (strain rate 10 mm/min, up to 50% strain; the tensile stiffness was normalized against cross-sectional area, please refer to the experimental section) was followed by stress relaxation for 2 min (double exponential model) and a final deformation until failure; due to the stress relaxation, the stress at failure (ultimate strength) values can be different (higher) than without the relaxation step. Please note that it is often impossible to precisely calculate stress, therefore we have preserved the most common terminology (stress-strain curve, stress relaxation), but we have actually employed force data, instead of stress. *B.* Normalized stiffness of 3D-seeded samples after 7 days of culture. *C.* Correlation between the increase in stiffness during contraction and the extent of contraction; the numbers in red report the fibrinogen concentration. *D.* Short (τ_1) and long (τ_2) relaxation times of 3D-seeded constructs as measured from the stress relaxation experiments. Before contracture, the short relaxation times of the softer gels were marginally larger than that of the hardest construct, but after contracture (red circles) no difference was apparent. *E.* Tensile strength measurements (stress at the point of rupture) of 3D-seeded constructs; no statistically significant effect can be seen, although the 12.5 mg/mL fibrin(ogen) may show a higher strength after contraction. (For interpretation of the references to colour in this figure legend, the reader is referred to the web version of this article.)

(Fig. 7A) increased 20–50% in the absence of TGF-β1, independent of the extent of bulk contracture, which is consistent with the lack of matrix orientation seen in SEM image of construct surfaces. A more significant increase was recorded in the presence of TGF-β1, and - differently from bulk measurements - the hardest constructs showed the highest increase (Fig. 7B). This is directly related to the mechanical behaviour of HDFa: control nanoindentation experiments performed selectively on cells showed that TGF-β1 makes HDFa harder (Fig. 7C, left) and that this process is specifically related to the hardening of stress fibres (Fig. 7C, centre), whose stiffer character and larger dimensions (Fig. 7C, right) tally well with the expression of α-SMA (Fig. 4A). Of note, the modulus values recorded for whole cells (Fig. 7C, left) are similar to those of the whole constructs. We previously noted contracture to be possible with matrix moduli below 2–2.5 kPa; in the light of this mechanical analysis, an alternative interpretation is that contracture might be limited by the very hardness of the cell. Indeed it seems reasonable that a cellular contractile machinery would be able to pull the surrounding matrix only when the latter is softer than the cell body.

In summary, at the level of whole constructs contracture and hardening are proportional, as it should be expected. However, the surface of the constructs behaves in a peculiar fashion, with a likely denser and more myofibroblastic cell population being directly responsible for (part of) the surface stiffening.

2.10. *Contracture in non-fibroblastic models*

Fibrosis accompanies a variety of inflammatory pathologies, which are not exclusively associated with fibroblastic phenotypes. Here, we have focused on muscle cells, with the aim to highlight the occurrence of irreversible contracture; myoblasts have been previously plated on or in fibrin-based gels [55–57] to generate myobundles, but always focusing on stimulated (reversible) contraction. However, contractures play an important role in pathologies such as muscular dystrophy: there, progressive muscle wastage is accompanied by its replacement with irreversibly contracted, fibrotic tissue, which hampers the contractile function of the residual healthy muscle [58,59]. The precise cellular etiology of fibrotic tissues in muscular dystrophies is still debated: a consensus exists that fibroblasts, adipocytes or fibro/adipogenic (platelet-derived growth factor (PDGFRA)-positive) precursor cells [60–62] are major players, but little is known regarding the direct participation of diseased muscle cells themselves. Here, we have employed human immortalized myoblasts, as models of healthy, diseased (dystrophic), and cured cells (dystrophic but genetically corrected via exon skipping of the dystrophin gene: the truncated but functional dystrophin can ameliorate muscle performance [63]).

In terms of the overall extent of contracture (Fig. 8A, larger graphs), all myoblasts and non-TGF-β1 stimulated fibroblasts were similar (40–50% contraction), both in 2D and in 3D.

Healthy and corrected myoblasts, however, clearly differed from

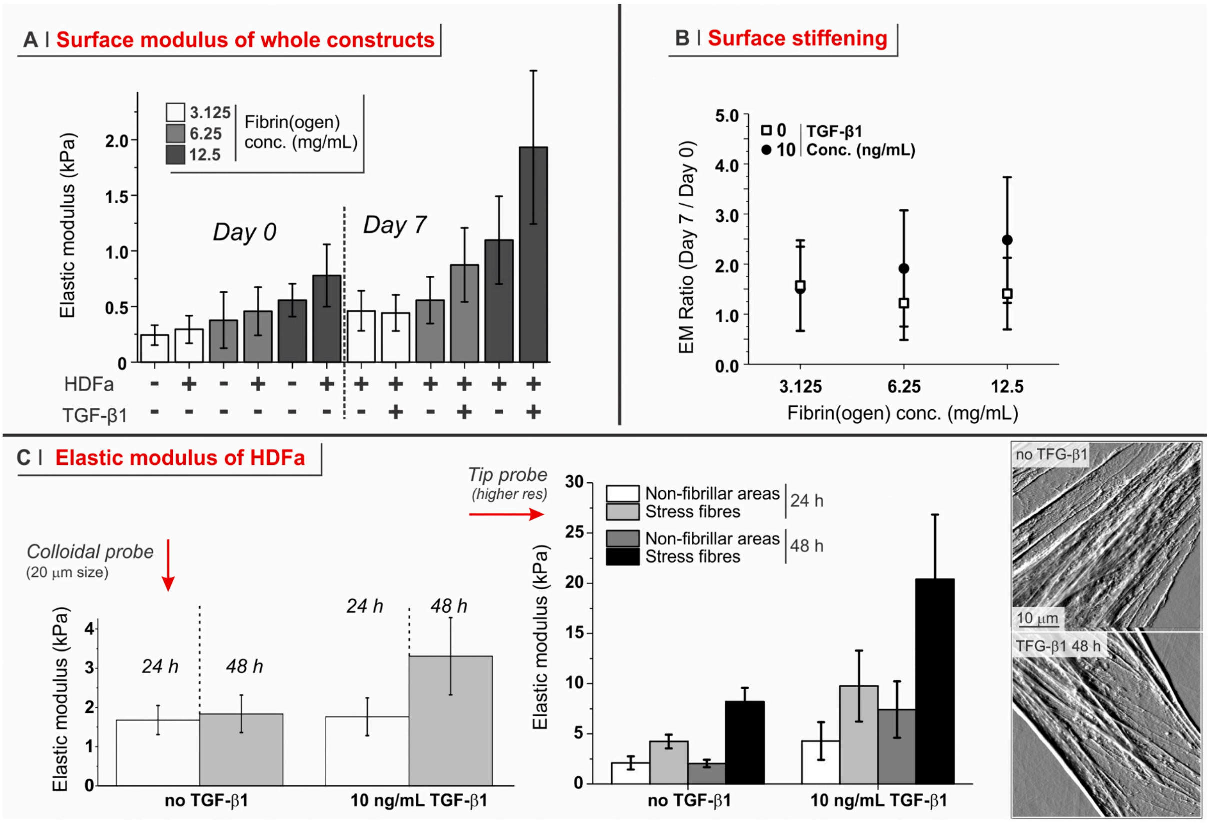

Fig. 7. *A.* The number average modulus values, obtained as reported in Supporting Information, Fig. 17SI, show that higher fibrin concentration, presence of TGF-β1 and the prolonged culture time all increased the surface stiffness of the constructs. *B.* The extent of stiffening is quantified reporting the fold increase in elastic modulus values between day 7 and day 0 (top, no TGF-β1), and with and without TGFβ1 at day 7 (below). *C.* HDFa were subjected to nanoindentation when cultured a planar substrate (TCPS, see Supporting Information, Section 1SI). *Left.* The modulus of the cells was measured using nanoindentation with a 2 m-sized colloidal probe, showing a considerably hardening upon a 48 h TGF-β1 treatment. *Centre.* Using an AFM tip-based nanoindentation, it is possible to selectively probe areas of the cell bodies corresponding to stress fibres or not. The corresponding force maps (see Supporting Information, Fig. 19SI) clearly show that most of the hardening is due to a > 2-fold elastic modulus increase in the areas corresponding to stress fibre areas. Please note that the elastic modulus values obtained with tip and colloidal probe-based nanoindentation are not necessarily comparable *Right.* Deflection images of HDFa on TCPS showing more developed stress fibres after a TGF-β1 treatment.

fibroblasts in the contraction kinetics: they acted more rapidly than HDFa in 2D-seeded constructs, and more slowly in 3D-seeded. Since 3D-seeding is more relevant for tissue fibrosis, this finding indicates a higher fibrotic potential for fibroblasts than healthy/corrected myoblasts, which is logical. On the other hand, dystrophic myoblasts always showed a rapid contracture, similar in speed to the other myoblasts in 2D, and to HDFa in 3D, indicating a higher propensity to 3D fibrotic processes for dystrophic cells than for their healthy/corrected counterparts. While on one hand this would tally with the actual pathology, on the other hand it would potentially suggest dystrophic cell direct participation in fibrosis.

Incidentally, both in 2D and in 3D these dystrophic cells showed a somehow reduced stain for sarcomeric myosin heavy chain (MHC), which is an early marker of terminal myogenic differentiation into myotubes and a key component of their reversible contraction machinery (Fig. 8B); this finding appears to confirm reports that dystrophic myoblasts in vitro may generate more immature myotubes [64], which are also less capable of stimulated, reversible contraction.

3. Conclusions

Our contracture wells recapitulate in vitro several features of tissue contractures, including the sensitivity to pro-fibrotic factors. HDFa can easily contract soft fibrin constructs ($E \leq 1.5$ kPa), but the extent of contraction is significantly increased through the use of TGF-1, which promotes HDFa differentiation to a myofibroblastic phenotype. Of note, while mechanical properties are a major determinant of contracture (harder construct – less contracture), they did not appear to affect the extent of myofibroblastic differentiation, i.e. cells do not appear to be 'more myofibroblastic' when on/in constructs more difficult to contract.

Further, our models allow us to differentiate two geometrically different contracture modes: interfacial (2D) processes occur when cells form and contract their own 'tissue' outside the constructs, and may be approximated to isotonic contractions. Bulk (3D) processes see cells pulling the matrix from within, and in the presence of constraints these phenomena may be considered isometric. These two modes, therefore, lend themselves to in vitro mimic, respectively, the fibrotic reaction around a non-infiltrated foreign body (e.g. capsular contracture around a silicone implant), or that within a tissue (e.g. that of a wound bed, or the formation of a Dupuytren nodule).

Some cell types may be more prone to participating in one or the other kind of contracture; for example, our models indicate that non-dystrophic myoblasts were more apt to 2D and less to 3D contracture, and the reverse applies to HDFa. Interestingly, dystrophic myoblasts appeared to be equally prone to both mechanisms, which may indicate a propensity of these diseased cells to be involved in fibrotic muscle degeneration.

In summary, we have validated 2D and 3D contracture models as medium-throughput and possibly automatable tests of the fibrotic capacity of various cell types, or for the pro- or anti-fibrotic effects that environmental cues can have on them. This can significantly increase the capacity of precisely predicting and fine tuning the efficacy of anti-

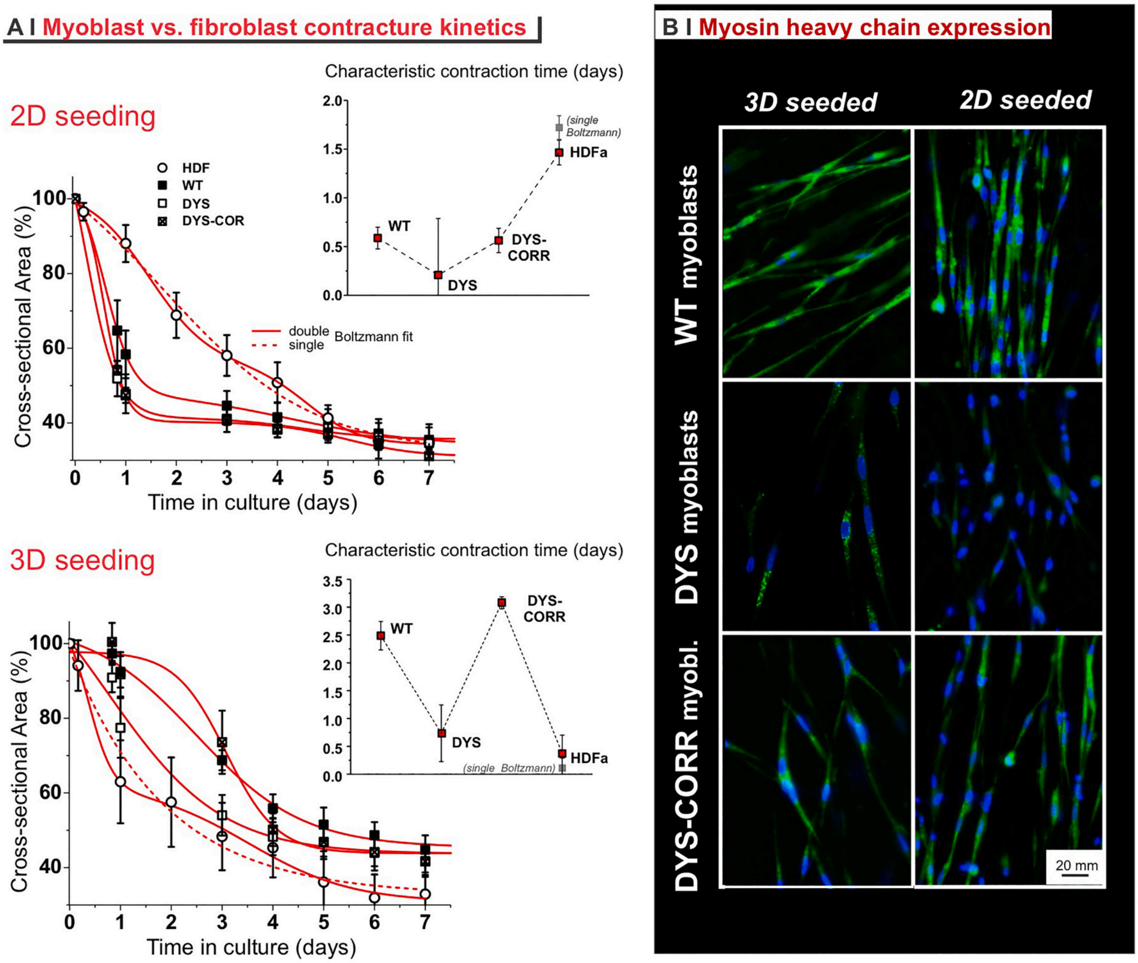

Fig. 8. WT: wild-type, healthy myoblasts. DYS: dystrophic myoblasts. DYS-CORR: dystrophic myoblasts where the dystrophin gene was engineered via exon skipping to provide a shorter but functional version of the protein. *A.* Contracture kinetics for 2D- (*left*) and 3D-seeded (*right*) constructs. The kinetics of myoblast-based constructs was typically bimodal; the slower component may be associated to differentiation and myotube formation. The myoblast data were correspondingly fitted with a double Boltzmann model (solid red lines) and the characteristic time of the more rapid component is presented in the insets; for comparison, HDFa (please note: without TBF-β1 treatment) data were fitted with the same model, but a single Boltzmann fitting provides virtually identical results (red dotted lines in the graphs, grey squares in the insets). *B.* Myoblasts 2D (above) and 3D (below) seeded on/in 6.25 mg/mL fibrin(ogen) were imaged for nuclei (DAPI, blue) and myosin heavy chain (green) at day 15, as a qualitative indication of myotube formation. Please note that a) the degree of fusion observed (2–3 nuclei per myotube) does not correspond with the level of myotube maturation required for dystrophin expression; b) the lower intensity observed for the myosin stain suggests a reduced capacity of fusion for dystrophic myoblasts when in/on a contracting matrix. (For interpretation of the references to colour in this figure legend, the reader is referred to the web version of this article.)

fibrotic therapy.

4. Materials and methods

4.1. Materials

Bovine fibrinogen (FG, F8630, Type I—S, α-chain Molecular weight (MW): 63.5 kDa, β-chain MW: 56 kDa, γ-chain MW: 47 kDa; soluble dimer MW: 340 kDa), bovine thrombin (≥1500 NIH units/mg protein), *N*-(2-(hydroxyethyl)piperazine-*N*′-(2-ethanesulfonic acid) (HEPES) and Pluronic F-127 (number average molecular weight 12.6 kDa) were purchased from Sigma-Aldrich (Gillingham, UK). Calcium chloride ($CaCl_2$) and sodium chloride (NaCl) were purchased from VWR International Ltd. (Leicester, UK). The poly(dimethylsiloxane) (PDMS) precursor Sylgard Type 184 was purchased by the Dow Chemical Corporation (Midland, MI, USA). Stainless steel 0.1 mm minutien pins were purchased from Fine Science Tools GmbH (Heidelberg, Germany).

4.2. Preparative operations

4.2.1. Preparation of fibrin gels

Fibrinogen stock solutions were prepared in HEPES-buffered saline (HBS: 20 mM HEPES, 150 mM NaCl, pH = 7.4) by slowly dissolving fibrinogen for 2 h at 37 °C under shaking, typically to obtain a concentration of 9.375, 18.75, 37.5 mg/mL. A stock HBS solution of thrombin and CaCl2 was produced by mixing equal volumes of 6 U/mL thrombin in HBS and of 120 mM CaCl2 in HBS. In a typical gelation experiment, 54 μL of this stock solution were mixed with 54 μL of a solution of fibrinogen at the appropriate concentration in HBS and with 54 μL of HBS, yielding final solutions 3.125, 6.25 or 12.5 mg/mL in fibrinogen, 1 U/mL in thrombin and 20 mM in CaCl2, which were allowed to react at 37 °C for 2 h.

4.2.2. Preparation of culture dishes and anchors

A PDMS mould was produced at the bottom of each well of a 12-well plate, by mixing the two components of Sylgard 184 (elastomer and curing agent, 10:1 weight ratio). The PDMS was cured at 60 °C for 45 min, yielding very viscous ('tacky'), but yet not completely cured materials. At this point, 13 mm diameter circular cover slip (previously treated with 3% *w/v* Pluronic F-127 for 30 min to reduce adhesion) was positioned at the centre of each well, then completing the curing at 60 °C for 30 min. The cover slips were finally removed to create a circular indent in the centre of the well, which typically is ~20 μm deep. The wells (including PDMS moulds) were then sterilized with pure ethanol for 30 min, and then treated for 2 h with a sterile-filtered (0.22 μm) 3% w/v Pluronic F127 solution to cover the PDMS substrates with a layer that prevents the adhesion of fibrin gels. Silk sutures (Mersilk Suture 3–0, Ethicon) of approximately 4 mm in length were pinned with minutien pins into the PDMS elastomer at a separating distance of 10 mm (as seen in Fig. 2B). Of note, both pins and sutures were sterilized with pure ethanol for 30 min prior use, and the plates were further sterilized under UV exposure overnight.

4.2.3. *Preparation of cell-seeded fibrin gels*

4.2.3.1. Fibroblast cell culture. During both expansion (on plastic substrates) and culture in/on fibrin constructs, adult human dermal fibroblasts (HDFa; C-013-5C, Cascade Biologics, Invitrogen, Paisley, UK; passage always <11) were cultured in high glucose Dulbecco's Modified Eagle Medium (DMEM, D6546, Sigma-Aldrich) supplemented with 10% *v*/v fetal bovine serum (FBS, Invitrogen), 1% v/v L-glutamine (Invitrogen) and 1% v/v penicillin/streptomycin solution (Sigma-Aldrich) (hereafter referred to as DMEM) and incubated at 37 °C/5% CO_2 under sterile conditions.

4.2.3.2. Myoblast cell culture. Immortalized human skeletal myoblasts from muscle biopsies of both healthy donors and DMD patients carrying a skippable mutation of exon 51 of the dystrophin gene (as developed by Mamchaoui et al. [65]; passage 4) were grown in SKM (Skeletal Muscle) medium, which consists of 80% high glucose DMEM and 20% 199 medium, supplemented with 20% FBS, 25 mg/mL Dexam (Sigma-Aldrich), 10 mg/mL gentamicin, 25 mg/mL fetuin and 1× insulin-transferrin-selenium-X (Thermo Fisher), 5 μg/mL human Fibroblast Growth Factor (hFGF) and 500 μg/mL recombinant human Endothelial Growth Factor (hEGF). Part of DMD myoblasts were genetically corrected with a lentiviral vector expressing a small nuclear RNA (U7) engineered to skip exon 51 of the dystrophin gene as originally described in De Angelis et al. [66]. Cells were passaged at 80% confluence. When seeded in/on constructs, myoblasts were left to adhere/spread for at least 24 h in SKM medium, and differentiation was then induced by replacing it with serum-free high-glucose DMEM, supplemented with 10 mg/mL gentamicin, 1× insulin-transferrin-selenium-X (kept for the whole duration of the experiments).

4.2.3.3. Cell-seeded constructs. Solutions of fibrinogen and thrombin (54 μL each, as described in Section 2.2.1) were mixed with 54 μL of either HBS (for 2D-seeded constructs) or a cell suspension in DMEM (for 3D-seeded constructs). 150 μL of gelling fibrinogen solutions (with or w/o cells) were pipetted within the circular indent in the anchored culture dishes ensuring good contact with the suture. Please note that the no fibrinolysis inhibitors were added. 2D constructs. After allowing gelation to occur at 37 °C for 2 h, 100 μL of a 70,000 cell/mL cell suspension in DMEM were carefully pipetted on to the gel surface, in order to obtain a surface density of 5000 HDFa/cm^2 or of 20,000 myoblasts/cm^2; myoblasts were used at a higher density for myoblasts to favour their fusion into myotubes. Cell attachment was allowed to occur at 37 °C for 4 h prior to the addition of 0.5 mL of DMEM. 3D constructs. Gelation and cell attachment were allowed to occur at 37 °C in a cell culture incubator, and 0.5 mL of DMEM was added after 4 h. A final cell density of 200,000 cells/mL was used for 3D constructs, unless otherwise stated.

The constructs were cultured for up to 7 days (up to 15 for myoblasts), changing the cell culture media at day 1, 2 and 4. In the experiments including TGF-β1 (recombinant human TGF-β1, ab50036, Abcam, Cambridge, UK) treatment, the DMEM used for the first two days after gelation contained 10 ng/mL of the growth factor, and was then replaced by normal DMEM for the remaining culture period. For cryosectioning, SEM, immunofluorescence and Picrosirius Red staining, at the end of the cell culture period the constructs were washed with PBS and fixed in 4% paraformaldehyde for 20 min at room temperature, then stored at 4 °C in PBS prior to any further analysis.

4.3. *Biological characterization*

4.3.1. *Viability tests*

Cell metabolic activity was quantified at days 1, 2, 4 and 7 of culture using resazurin reduction with the addition Deep Blue Cell Viability Kit (BioLegend) in a 1:10 ratio with cell culture media, measuring fluorescence intensity of supernatants with a Synergy 2 multi-mode BIOTek microplate reader 4 h after the addition of the staining agent. After each measure, cells were washed with DMEM and then fresh cell culture medium was added to wells. Moreover, a live/dead cell staining kit (Calcein-AM/ propidium iodide-based 04511 Cellstain double staining kit, Sigma Aldrich) was used following the manufacturer's instructions to study cell viability at day 7. Images were acquired on a Leica DMI6000B inverted microscope with a 20× objective and processed with ImageJ.

4.3.2. *Cryosectioning*

3D-seeded, fixed constructs went through sequential incubations (1 h, RT) in 7.5%, 15% and finally 30% *w/v* sucrose in PBS solutions, in order to prevent the formation of ice crystals during freezing. Sutures were carefully removed, and the constructs were embedded in Tissue Tek OCT compound before being frozen in liquid nitrogen-cooled isopentane. Frozen samples were sectioned with a Leica CM3050 S cryostat to a thickness of 10 μm and mounted on microscope slides.

4.3.3. *Immunofluorescence*

4.3.3.1. α-Smooth muscle actin imaging. Fixed samples were permeabilized with 0.1% Triton X-100 in phosphate buffered saline (PBS) for 3 min followed by blocking with 5% w/v bovine serum albumin (BSA) in PBS overnight at 4 °C. α-Smooth muscle actin was stained with an anti-αSMA antibody (mouse monoclonal, A2547, Sigma Aldrich) at a 1:200 dilution in PBS containing 1% w/v BSA (PBS-BSA) for 60 min followed by a secondary Alexa Fluor® 488-conjugated antibody (ab150113, Abcam) at a 1:500 dilution in PBS-BSA for 60 min. F-actin fibres were stained using Alexa Fluor® 594-conjugated phalloidin (Invitrogen) in a 1:200 dilution in PBS-BSA for 60 min. Nuclei were stained with 1 μg/mL DAPI (4′ 6-diamidino-2-phenylindole) in PBS for 5 min. All the above incubation steps were conducted at room temperature and in the dark, washing the samples 3 times with PBS between each step. Samples were detached from the PDMS substrate and placed on a glass coverslip, whilst ensuring the samples remained hydrated, prior to imaging on an inverted Leica SP8 confocal microscope with a 40× oil immersion objective lens. Maximum intensity projection was used on z-stacks of images to accommodate for either surface curvature and sampling a volume of the constructs. 3D projection images were generated using IMARIS software based on z-stacks of confocal images acquired using a 10× objective lens.

4.3.3.2. Evaluation of cell alignment. Fixed fibrin construct samples were stained with DAPI and Alexa Fluor® 488-conjugated phalloidin (Invitrogen) using the procedure as described in the previous section. Samples were detached from the PDMS substrate and placed on a glass coverslip whilst ensuring the samples remained hydrated prior to imaging on an inverted Leica SP5 confocal microscope with a x40 oil immersion lens. Note that 2D-seeded constructs were placed top-side down to ensure the cells were within the focal length of the lens. By taking a maximum intensity projection of a z-stack of images it was possible to overcome the curvature of the constructs to obtain a 2D image for each region of interest. The F-actin images were subsequently imported into SOAX, an open source fibre image analysis software [67]. This allowed the quantification of the direction of the individual F-actin filament segments which was characterized by an order parameter $S = (3 < cos^2\theta > - 1)/2$, where θ is the angle between an actin fibre segment and the primary axis of the filament direction, which macroscopically equates to the inter-suture axis. S = 1 represents complete alignment of all the filaments with the primary axis; S = 0 equates to random alignment; S = −0.5 is equivalent to complete anti-alignment of the filaments with the primary axis.

4.3.3.3. Myosin heavy chain imaging. Fixed myoblast construct samples (day 15) were washed with 0.2% Triton X-100 and 1% *w/v* BSA in phosphate buffered saline (BSA-PBST) for 30 min followed by blocking with 10% *v*/v fetal bovine serum in PBS for 30 min. Cells were stained with anti-myosin heavy chain (MHC) (MF-20, Developmental Studies Hybridoma Bank, Univ. of Iowa, Iowa City, IA) in BSA-PBST overnight at 4 °C. Samples were subsequently washed 3 times for 15 min with PBST prior to the incubation with secondary Alexa 488 anti-mouse antibody (Invitrogen). After further 2 washings in PBST for 15 mins each, nuclei were counterstained with DAPI (1:1000 in BSA-PBS, Sigma Aldrich) for 5 min and similarly washed again. Fluorescence images were subsequently acquired on a Zeis Observer D1 inverted microscope (Zeiss, Oberkochen, Germany) equipped with a Zeiss AxioCamMRm and Axiovision Software. Maximum intensity projection was used on z-stacks of images to accommodate for either surface curvature and sampling a volume of the constructs.

4.3.4. Collagen histochemical analysis (Picrosirius Red staining)

Picrosirius red staining was performed on 10 μm-thick sections of fixed constructs after 7 days of culture to demonstrate fibrillar collagen production. Samples were immersed in a Fast Green counterstain, consisting of 0.1% w/v Picrosirius red and 0.1% Fast Green stains in saturated picric acid for 1 h, then dehydrated and mounted prior to imaging with a 3D Histec Pannoramic250 slide scanner.

4.3.5. Quantitative reverse transcription PCR (qRT-PCR)

Fibrin gel constructs were extracted from their anchors and homogenized with the mechanical action of scissors. Each replicate consisted of two constructs in a single tube to ensure sufficient RNA could be extracted. TRIzol (500 μL) was added to each tube and incubated at room temperature for 5 min. At this point, samples could be frozen at −80 °C prior to further extraction. Chloroform (200 μL) was added to each sample that were subsequently mixed by inversion for 15 s, incubated at 15 min at room temperature then centrifuged at 12,000*g* for 15 min at 4 °C. Following this, the clear aqueous layer was carefully extracted from each sample and placed into a clean Eppendorf tube. Isopropanol (250 μL) was added to each sample that were incubated for 10 min at room temperature prior to being centrifuged at 4 °C for 10 min. After discarding the supernatant, 500 μl of 70% ethanol was added to each sample that were then centrifuged for 5 min at 4 °C. The supernatant was subsequently discarded, and the samples were left to dry at room temperature for 10 min to dry before the addition of 20 μL of RNAse free water. The concentration of the extracted RNA was quantified on a NanoDrop 1000 Spectrophotometer. For reverse transcription, a Thermo Scientific RevertAid RT Kit was used by following the manufacturer's instructions to produce cDNA from 1 μg of each RNA sample. These samples were subsequently treated with FastStart Essential DNA Green Master Mix (Roche) following the manufacturer's instruction for a quantitative SYBR Green I-based real-time PCR using the LightCycler® 96 Instrument. Primers: ACTA2 for αSMA (SY180520856), COL1A1 for collagen 1 (SY 180520856–065), and ACTB for β-Actin (SY151136672) was used as an endogenous control.

4.4. Material characterization

4.4.1. Contracture analysis

Contracture was quantified through two parameters: cross-sectional area and aspect ratio. The former was measured on top-down Fig.s through tracing and area evaluation, the latter was calculated as the inter-suture distance divided by the maximum width in the orthogonal direction. Calculations were performed in ImageJ and data were normalized against their initial values. For HDFa the cross-sectional area, *A(t),* was fitted with a Boltzmann sigmoidal distribution: $A(t) = \frac{A_i - A_f}{1 - e^{\frac{(t - t_0)}{dt}}} - A_f$, where A_i is the initial cross-sectional area (normalized to 100%), A_f is the final cross-sectional area, *dt* is the slope and *t₀* is the centre of the sigmoidal fit, which was used as the characteristic time the phenomenon. For myoblasts a biphasic behaviour was apparent, and was fitted with a double Boltzmann model with equation $A(t) = A_f + (A_i - A_f)\left(\frac{p}{1 - e^{\frac{(t - t_1)}{dt_1}}} + \frac{1 - p}{1 - e^{\frac{(t - t_2)}{dt_2}}}\right)$. The parameters are identical to single Boltzmann, with *p* added to account for the fractional amount of initial contracture (phase 1).

The ImageJ package TrakEM2 [68] was used for the registration of the sequential images of the constructs at each day to accommodate any variation in the angle of imaging, which was critical for accurate aspect ratio measurements and contracture movie generation.

4.4.2. SEM analysis

Cell-seeded fibrin constructs, prepared and cultured for 7 days as described in Section 2.2.3, were fixed for 2 h in 2% glutaraldehyde in 0.1 M cacodylate buffer at room temperature. After fixation, the samples were washed thrice with the same buffer and post fixed for 1 h in 1% *w/v* osmium tetroxide in 0.1 M cacodylate buffer. After several washes with MilliQ water, samples were subsequently dehydrated in a graded ethanol series, 1:1 ethanol:hexamethyldisilazane (HMDS) and pure HMDS, and air-dried overnight. Dried samples were then mounted on stubs and coated with gold. In order to image the internal part of the constructs, the stubs (with the samples mounted on them) were immersed in liquid nitrogen and a fracture was applied in order to have a clean cross-section of the constructs. The morphology of each sample was characterized using a JEOL JSM-6490LA Scanning Electron Microscope (SEM) equipped with a tungsten filament and operating at 10KV of accelerating voltage.

4.4.3. Mechanical testing

4.4.3.1. Compression. Compressive measurements were used to characterize the matrices and were performed on non-cell-containing gels, which therefore all had identical dimensions. The Young's moduli of cylindrically shaped (height: 3 mm; diameter: 8 mm; no cell) gels were determined via compression tests performed on a TA. XT. Plus texture analyser (Stable Micro Systems, Godalming, Surrey, UK) at room temperature in air with a compression speed of 0.1 mm/s up to 5% strain, starting the measurement from a non-contact position (about 2 mm above the gel surface).

4.4.3.2. Shear rheology. Rheological measurements were conducted as described by Valdivieso et al. [34]. Briefly, precursor gel solutions were placed between the parallel plates of a Bohlin Instruments Gemini rheometer (Malvern Instruments Ltd., Malvern, UK) and were incubated at 37 °C for 2 h for gelation to occur prior to taking measurements in a stress-controlled mode (upper plate diameter 20 mm, plate separation 100 μm).

4.4.3.3. Tensile testing. These measurements were performed on constructs carefully removed from the PDMS moulds and clamped securely in an Instron 3365 uniaxial testing machine at a clamp separation distance of 6–10 mm. These constructs underwent a variable degree of contraction and therefore also had variable lateral dimensions (hence the data are presented as stiffness rather than modulus, see below). Samples were subjected to a 10 mm/min increase in strain up to 50% elongation to obtain a *stress-strain curve*, then held at a constant strain for 120 s to perform *stress relaxation* experiments and finally subjected to a further 10 mm/min strain increase until mechanical failure, in order to determine their *tensile strength*. The samples are exposed to air for about 5 min, a time assumed to be short enough to exclude any significant dehydration at room temperature. The stress relaxation data were fitted with a double exponential function, as expected for a 4-element Maxwell model of 2 sets of a spring and dashpot in series. The normalized stiffness (slope of the stress-strain curve divided by the transverse sectional area at half-length) of the samples was determined by calculating the slope of the initial stress-strain curve within the 2–10% linear elongation range. Please note that normalized stiffness is not a modulus, albeit it is calculated in the same fashion (stress divided by transverse sectional area). The main point is that the sectional area can vary significantly along the main axis of the constructs, where a modulus can be correctly calculated only if it were homogeneous; additionally, a modulus value may suggest that the cell-containing materials are internally homogeneous, while in reality they are rather heterogeneous, due to higher cell density closer to the surface.

4.4.4. *Nanoindentation*

Nanoindentation studies were performed in liquid conditions (constructs immersed in 10 mM PBS buffer, pH = 7.4) on samples containing living cells using a Molecular Force Probe 3D AFM (Model MFP-3D, Asylum Research – Oxford Instruments, UK). Anchored constructs were analyzed with/without cells (3D) at day 0 (2–3 h after their fibrin gelation) and with cells ± TGFβ1 at day 7. sQUBE (Bickenbach, Germany supplied by Windsor Scientific LTD, Berkshire, UK) colloidal probes (CP-PNPL-SiO-A SiO_2 particles attached on a cantilever) were used for all measurements. The nominal spring constant, particle diameter, cantilever length and probe resonance frequency were 0.08 N/m, 2 μm, 200 μm and 15 Hz, respectively. Two probes were used for this analysis, with their actual spring constants determined by the thermal noise method as 0.04 N/m and 0.06 N/m. For indentation on cells, see Supporting Information, section 1SI.

On each sample analyzed, several force maps were acquired performing 210 indentation curves within a 20 μm × 20 μm area (spatial resolution: 1.90 μm^2). The relative elastic modulus was calculated by fitting the force-indentation data with the Hertz sphere model (Hertz sphere-on-flat model), where E_s, ν_s, R_{tip} and h are the relative elastic modulus of the surface, the Poisson's ratio of the samples ($\nu = 0.7$)[41], the radius of the sphere attached to the cantilever ($R = 1$ μm) and the displacement of the specimen, respectively.

4.4.5. *Statistical analysis*

Contraction or mechanical data are presented as mean and standard error on 6 samples from 2 independent preparations, unless otherwise stated. The levels of significance * - $p < 0.05$, ** - $p < 0.01$, *** - $p < 0.001$ were obtained through two-way ANOVA (GraphPad PRISM 8).

CRediT authorship contribution statement

Iwan Vaughn Roberts (IVR): design of the contracture well, all experiments of HDFa-mediated contracture, including mechanical characterization, manuscript preparation.

Roberto Donno (RD): nanoindentation and electron microscopy experiments.

Francesco Galli (FG): myoblast culture (incl. Genetic correction) and myoblast-mediated contraction experiments.

Christopher Yusef Leon Valdivieso (CYLV): compression and shear rheology experiments.

Alessandro Siani (AS): HDFa culture for nanoindentation experiments and contribution to nanoindentation experiments.

Giulio Cossu (GC): supervision of FG and co-supervision of IVR, in particular myoblast experiments.

Annalisa Tirella (AT): co-supervision of IVR and assistance to cell culture and mechanical experiments.

Nicola Tirelli (NT): general supervision, conceptualization, funding, manuscript preparation.

Data availability

All of the data reported in this work are available upon request.

Declaration of competing interest

The authors declare that they have no known competing financial interests or personal relationships that could have appeared to influence the work reported in this paper.

Acknowledgements

The authors wish to acknowledge the funding provided by the Engineering and Physical Sciences Research Council (EPSRC) and Medical Research Council (MRC) to the Centre for Doctoral Training in Regenerative Medicine (EP/L014904/1), which supported the PhD project of Dr. Iwan Roberts, and B) the Consejo Nacional de Ciencia y Tecnología (CONACYT), which supported the PhD project of Dr. Christopher Yusef Leon Valdivieso (educational scholarship number 372904). The Bioimaging Facility microscopes used in this study were purchased with grants from BBSRC, Wellcome Trust and the University of Manchester Strategic Fund. The Histology Facility equipment used in this study was purchased through the University of Manchester Strategic Fund. Special thanks to Peter Walker, Luca Ceseracciu and Simone Lauciello for their assistance on histology, tensile testing and SEM, respectively.

Appendix A. Supplementary data

Supplementary data to this article can be found online at https://doi.org/10.1016/j.msec.2022.112661.

References

[1] J.M. Snowden, Wound closure: an analysis of the relative contributions of contraction and epithelialization, J. Surg. Res. 37 (6) (1984) 453–463.

[2] T. Mammoto, D.E. Ingber, Mechanical control of tissue and organ development, Development 137 (9) (2010) 1407.

[3] D. Wolfram, A. Tzankov, P. PÜLzl, H. Piza-Katzer, Hypertrophic scars and keloids—a review of their pathophysiology, risk factors, and therapeutic management, Dermatol. Surg. 35 (2) (2009) 171–181.

[4] J.E. Puche, Y. Saiman, S.L. Friedman, Hepatic stellate cells and liver fibrosis, Compr. Physiol. 3 (4) (2013) 1473–1492.

[5] C. Lossing, H.A. Hansson, Peptide growth-factors and myofibroblasts in capsules around human breast implants, PlastReconstr. Surg. 91 (7) (1993) 1277–1286.

[6] A.M. Oosterwijk, L.J. Mouton, H. Schouten, L.M. Disseldorp, C.P. van der Schans, M.K. Nieuwenhuis, Prevalence of scar contractures after burn: a systematic review, Burns 43 (1) (2017) 41–49.

[7] R. Lanting, D.C. Broekstra, P.M.N. Werker, E.R. van den Heuvel, A systematic review and meta- analysis on the prevalence of dupuytren disease in the general population of Western countries, Plast. Reconstr. Surg. 133 (3) (2014) 593–603.

[8] V.S. Nirmalanandhan, M.S. Levy, A.J. Huth, D.L. Butler, Effects of cell seeding density and collagen concentration on contraction kinetics of mesenchymal stem cell-seeded collagen constructs, Tissue Eng. 12 (7) (2006) 1865–1872.

[9] J.Z. Paxton, U.N.G. Wudebwe, A. Wang, D. Woods, L.M. Grover, Monitoring sinew contraction during formation of tissue-engineered fibrin-based ligament constructs, Tissue Eng. A 18 (15–16) (2012) 1596–1607.

[10] Y.C. Huang, R.G. Dennis, L. Larkin, K. Baar, Rapid formation of functional muscle in vitro using fibrin gels, J. Appl. Physiol. 98 (2) (2005) 706–713.

[11] C. O'Rourke, R.A.L. Drake, G.W.W. Cameron, A. Jane Loughlin, J.B. Phillips, Optimising contraction and alignment of cellular collagen hydrogels to achieve reliable and consistent engineered anisotropic tissue, J. Biomater. Appl. 30 (5) (2015) 599–607.

[12] C.R. Lee, H.A. Breinan, S. Nehrer, M. Spector, Articular cartilage chondrocytes in type I and type II collagen-GAG matrices exhibit contractile behavior in vitro, Tissue Eng. 6 (5) (2000) 555–565.
[13] W.S. Toh, T.C. Lim, M. Kurisawa, M. Spector, Modulation of mesenchymal stem cell chondrogenesis in a tunable hyaluronic acid hydrogel microenvironment, Biomaterials 33 (15) (2012) 3835–3845.
[14] D.O. Visscher, E.J. Bos, M. Peeters, N.V. Kuzmin, M.L. Groot, M.N. Helder, P.P. M. van Zuijlen, Cartilage tissue engineering: preventing tissue scaffold contraction using a 3D-printed polymeric cage, Tissue Eng. CMeth. 22 (6) (2016) 573–584.
[15] I.V. Roberts, D. Bukhary, C.Y.L. Valdivieso, N. Tirelli, Fibrin matrices as (Injectable) biomaterials: formation, clinical use, and molecular engineering, Macromol. Biosci. 20 (1) (2020).
[16] W.D. Spotnitz, Fibrin sealant: past, present, and future: a brief review, World J. Surg. 34 (4) (2010) 632–634.
[17] A. Noori, S.J. Ashrafi, R. Vaez-Ghaemi, A. Hatamian-Zaremi, T.J. Webster, A review of fibrin and fibrin composites for bone tissue engineering, Int. J. Nanomedicine 12 (2017) 4937–4961.
[18] D.B. Cines, T. Lebedeva, C. Nagaswami, V. Hayes, W. Massefski, R.I. Litvinov, L. Rauova, T.J. Lowery, J.W. Weisel, Clot contraction: compression of erythrocytes into tightly packed polyhedra and redistribution of platelets and fibrin, Blood 123 (10) (2014) 1596.
[19] S. Kattula, J.R. Byrnes, A.S. Wolberg, Fibrinogen and fibrin in hemostasis and thrombosis, Arterioscler. Thromb. Vasc. Biol. 37 (3) (2017) e13–e21.
[20] O.V. Kim, R.I. Litvinov, M.S. Alber, J.W. Weisel, Quantitative structural mechanobiology of platelet-driven blood clot contraction, Nat. Commun. 8 (1) (2017) 1274.
[21] V.F. Achterberg, L. Buscemi, H. Diekmann, J. Smith-Clerc, H. Schwengler, J. J. Meister, H. Wenck, S. Gallinat, B. Hinz, The Nano-scale mechanical properties of the extracellular matrix regulate dermal fibroblast function, J. Invest. Dermatol. 134 (7) (2014) 1862–1872.
[22] A.J. Booth, R. Hadley, A.M. Cornett, A.A. Dreffs, S.A. Matthes, J.L. Tsui, K. Weiss, J.C. Horowitz, V.F. Fiore, T.H. Barker, B.B. Moore, F.J. Martinez, L.E. Niklason, E. S. White, Acellular normal and fibrotic human lung matrices as a culture system for in vitro investigation, Am. J. Resp. Crit. Care 186 (9) (2012) 866–876.
[23] A.J. Engler, M.A. Griffin, S. Sen, C.G. Bönnemann, H.L. Sweeney, D.E. Discher, Myotubes differentiate optimally on substrates with tissue-like stiffness, J. Cell Biol. 166 (6) (2004) 877.
[24] P.M. Gilbert, K.L. Havenstrite, K.E.G. Magnusson, A. Sacco, N.A. Leonardi, P. Kraft, N.K. Nguyen, S. Thrun, M.P. Lutolf, H.M. Blau, Substrate elasticity regulates skeletal muscle stem cell self-renewal in culture, Science 329 (5995) (2010) 1078.
[25] W.C. Yeh, P.C. Li, Y.M. Jeng, H.C. Hsu, P.L. Kuo, M.L. Li, P.M. Yang, P.H. Lee, Elastic modulus measurements of human liver and correlation with pathology, Ultrasound Med. Biol. 28 (4) (2002) 467–474.
[26] C.G. Elliott, J. Wang, X. Guo, S.W. Xu, M. Eastwood, J. Guan, A. Leask, S. J. Conway, D.W. Hamilton, Periostin modulates myofibroblast differentiation during full-thickness cutaneous wound repair, J. Cell Sci. 125 (Pt 1) (2012) 121–132.
[27] T. Kobayashi, X.D. Liu, H.J. Kim, T. Kohyama, F.Q. Wen, S. Abe, Q.H. Fang, Y. K. Zhu, J.R. Spurzem, P. Bitterman, S.I. Rennard, TGF-beta 1 and serum both stimulate contraction but differentially affect apoptosis in 3D collagen gels, Respir. Res. 6 (2005).
[28] B. Piersma, S. de Rond, P.M.N. Werker, S. Boo, B. Hinz, M.M. van Beuge, R.A. Bank, YAP1 is a driver of myofibroblast differentiation in Normal and diseased fibroblasts, Am. J. Pathol. 185 (12) (2015) 3326–3337.
[29] M.J. Reed, R.B. Vernon, I.B. Abrass, E.H. Sage, TGF-β1 induces the expression of type I collagen and SPARC, and enhances contraction of collagen gels, by fibroblasts from young and aged donors, J. Cell. Physiol. 158 (1) (1994) 169–179.
[30] T.N. Snyder, K. Madhavan, M. Intrator, R.C. Dregalla, D. Park, A fibrin/hyaluronic acid hydrogel for the delivery of mesenchymal stem cells and potential for articular cartilage repair, J. Biol. Eng. 8 (2014) 10.
[31] D.M. Burmeister, D.C. Roy, S.C. Becerra, S. Natesan, R.J. Christy, In situ delivery of fibrin-based hydrogels prevents contraction and reduces inflammation, J. Burn Care Res. 39 (1) (2018) 40–53.
[32] B. Li, F. Li, L. Ma, J. Yang, C. Wang, D. Wang, C. Gao, Poly(lactide-co-glycolide)/fibrin gel construct as a 3D model to evaluate gene therapy of cartilage in vivo, Mol. Pharm. 11 (7) (2014) 2062–2070.
[33] S. Calve, R.G. Dennis, P.E. Kosnik, K. Baar, K. Grosh, E.M. Arruda, Engineering of functional tendon, Tissue Eng. 10 (5–6) (2004) 755–761.
[34] C.Y. Leon-Valdivieso, J. Wedgwood, E. Lallana, R. Donno, I. Roberts, M. Ghibaudi, A. Tirella, N. Tirelli, Fibroblast migration correlates with matrix softness. A study in knob-hole engineered fibrin, APL Bioeng. 2 (3) (2018) 19.
[35] M.L. Bayer, C.Y.C. Yeung, K.E. Kadler, K. Qvortrup, K. Baar, R.B. Svensson, S. P. Magnusson, M. Krogsgaard, M. Koch, M. Kjaer, The initiation of embryonic-like collagen fibrillogenesis by adult human tendon fibroblasts when cultured under tension, Biomaterials 31 (18) (2010) 4889–4897.
[36] J.Z. Paxton, L.M. Grover, K. Baar, Engineering an in vitro model of a functional ligament from bone to bone, Tissue Eng. A 16 (11) (2010) 3515–3525.
[37] A. Akhmetshina, K. Palumbo, C. Dees, C. Bergmann, P. Venalis, P. Zerr, A. Horn, T. Kireva, C. Beyer, J. Zwerina, H. Schneider, A. Sadowski, M.O. Riener, O. A. MacDougald, O. Distler, G. Schett, J.H.W. Distler, Activation of canonical Wnt signalling is required for TGF-beta-mediated fibrosis, Nat. Commun. 3 (2012) 12.
[38] A. Vallee, Y. Lecarpentier, TGF-beta in fibrosis by acting as a conductor for contractile properties of myofibroblasts, Cell Biosci. 9 (1) (2019) 15.
[39] Y. Nakamura, S. Hirano, K. Suzuki, K. Seki, T. Sagara, T. Nishida, Signaling mechanism of TGF-β1–Induced collagen contraction mediated by bovine trabecular meshwork cells, Invest. Ophth. Vis. Sci. 43 (11) (2002) 3465–3472.
[40] J.H. Kim, Y.-J. Seol, I.K. Ko, H.-W. Kang, Y.K. Lee, J.J. Yoo, A. Atala, S.J. Lee, 3D bioprinted human skeletal muscle constructs for muscle function restoration, Sci. Rep.-UK 8 (1) (2018) 12307.
[41] C.-Y.C. Yeung, C. Lallyett, Y. Lu, E.G. Canty-Laird, K.E. Kadler, L.a.H. Zeef, Chick tendon fibroblast transcriptome and shape depend on whether the cell has made its own collagen matrix, Sci. Rep.-UK 5 (May) (2015) 13555.
[42] A. Siani, G. Robert-Nicoud, F. Cellesi, N. Tirelli, Quantitative descriptors for the effect of nature/mechanical properties of solid substrates on fibroblast morphology, J. Appl. Biomater. Func. 10 (3) (2012) 265–272.
[43] A. Siani, N. Tirelli, Myofibroblast differentiation: main features, biomedical relevance, and the role of reactive oxygen species, Antiox. Redox Sign. 21 (5) (2013) 768–785.
[44] P.T. Ten Dijke, M.J. Goumans, F. Itoh, S. Itoh, Regulation of cell proliferation by Smad proteins, J. Cell. Physiol. 191 (1) (2002) 1–16.
[45] A. Siani, R.R. Khaw, O.W.G. Manley, A. Tirella, F. Cellesi, R. Donno, N. Tirelli, Fibronectin localization and fibrillization are affected by the presence of serum in culture media, Sci. Rep.-UK 5 (2015) 10.
[46] A. Desmoulière, A. Geinoz, F. Gabbiani, G. Gabbiani, Transforming growth factor-beta 1 induces alpha-smooth muscle actin expression in granulation tissue myofibroblasts and in quiescent and growing cultured fibroblasts, J. Cell Biol. 122 (1) (1993) 103.
[47] G. Gabbiani, The myofibroblast in wound healing and fibrocontractive diseases, J. Pathol. 200 (4) (2003) 500–503.
[48] A. Leask, Potential therapeutic targets for cardiac fibrosis TGF beta, angiotensin, endothelin, CCN2, and PDGF, Partners in Fibroblast Activation, Circ. Res. 106 (11) (2010) 1675–1680.
[49] V. Singh, F.L. Barbosa, A.A.M. Torricelli, M.R. Santhiago, S.E. Wilson, Transforming growth factor beta and platelet-derived growth factor modulation of myofibroblast development from corneal fibroblasts in vitro, Exp. Eye Res. 120 (2014) 152–160.
[50] I.A. Darby, N. Zakuan, F. Billet, A. Desmouliere, The myofibroblast, a key cell in normal and pathological tissue repair, Cell. Mol. Life Sci. 73 (6) (2016) 1145–1157.
[51] S.M. Lin, L.X. Gu, Influence of crosslink density and stiffness on mechanical properties of type I collagen gel, Materials 8 (2) (2015) 551–560.
[52] J.A. Stella, J. Liao, Y. Hong, W.D. Merryman, W.R. Wagner, M.S. Sacks, Tissue-to-cellular level deformation coupling in cell micro-integrated elastomeric scaffolds, Biomaterials 29 (22) (2008) 3228–3236.
[53] S.J. Heo, N.L. Nerurkar, B.M. Baker, J.W. Shin, D.M. Elliott, R.L. Mauck, Fiber stretch and reorientation modulates mesenchymal stem cell morphology and fibrous gene expression on oriented nanofibrous microenvironments, Ann. Biomed. Eng. 39 (11) (2011) 2780–2790.
[54] P. Kurki, I. Virtanen, The detection of smooth-muscle muscle antibodies reacting with intermediate filaments of desmin type, J. Immunol. Methods 76 (2) (1985) 329–335.
[55] M.A. Bakooshli, E.S. Lippmann, B. Mulcahy, N. Iyer, C.T. Nguyen, K. Tung, B. A. Stewart, H. van den Dorpel, T. Fuehrmann, M. Shoichet, A. Bigot, E. Pegoraro, H. Ahn, H. Ginsberg, M. Zhen, R.S. Ashton, P.M. Gilbert, A 3D culture model of innervated human skeletal muscle enables studies of the adult neuromuscular junction, eLife 8 (2019).
[56] L. Madden, M. Juhas, W.E. Kraus, G.A. Truskey, N. Bursac, Bioengineered human myobundles mimic clinical responses of skeletal muscle to drugs, eLife 4 (2015).
[57] N.R.W. Martin, S.L. Passey, D.J. Player, A. Khodabukus, R.A. Ferguson, A. P. Sharples, V. Mudera, K. Baar, M.P. Lewis, Factors affecting the structure and maturation of human tissue engineered skeletal muscle, Biomaterials 34 (23) (2013) 5759–5765.
[58] Y. Kharraz, J. Guerra, P. Pessina, A.L. Serrano, P. Munoz-Canoves, Understanding the process of fibrosis in duchenne muscular dystrophy, Biomed. Res. Int. 2014 (2014).
[59] C.J. Mann, E. Perdiguero, Y. Kharraz, S. Aguilar, P. Pessina, A.L. Serrano, P. Munoz-Canoves, Aberrant repair and fibrosis development in skeletal muscle, Skelet. Muscle 1 (2011).
[60] S.S. Gao, S.N. Chen, C. Di Nardo, R. Lombardi, Arrhythmogenic cardiomyopathy and skeletal muscle dystrophies: shared histopathological features and pathogenic mechanisms, Front. Physiol. 11 (2020).
[61] A. Uezumi, S. Fukada, N. Yamamoto, M. Ikemoto-Uezumi, M. Nakatani, M. Morita, A. Yamaguchi, H. Yamada, I. Nishino, Y. Hamada, K. Tsuchida, Identification and characterization of PDGFR alpha(+) mesenchymal progenitors in human skeletal muscle, Cell Death Dis. 5 (2014).
[62] A. Uezumi, T. Ito, D. Morikawa, N. Shimizu, T. Yoneda, M. Segawa, M. Yamaguchi, R. Ogawa, M.M. Matev, Y. Miyagoe-Suzuki, S. Takeda, K. Tsujikawa, K. Tsuchida, H. Yamamoto, S. Fukada, Fibrosis and adipogenesis originate from a common mesenchymal progenitor in skeletal muscle, J. Cell Sci. 124 (21) (2011) 3654–3664.
[63] P. Roy, F. Rau, J. Ochala, J. Messeant, B. Fraysse, J. Laine, O. Agbulut, G. Butler-Browne, D. Furling, A. Ferry, Dystrophin restoration therapy improves both the reduced excitability and the force drop induced by lengthening contractions in dystrophic mdx skeletal muscle, Skelet. Muscle 6 (2016).
[64] A.P. Nesmith, M.A. Wagner, F.S. Pasqualini, B.B. O'Connor, M.J. Pincus, P. R. August, K.K. Parker, A human in vitro model of duchenne muscular dystrophy muscle formation and contractility, J. Cell Biol. 215 (1) (2016) 47–56.
[65] K. Mamchaoui, C. Trollet, A. Bigot, E. Negroni, S. Chaouch, A. Wolff, P.K. Kandalla, S. Marie, J. Di Santo, J.L. St Guily, F. Muntoni, J. Kim, S. Philippi, S. Spuler, N. Levy, S.C. Blumen, T. Voit, W.E. Wright, A. Aamiri, G. Butler-Browne, V. Mouly, Immortalized pathological human myoblasts: towards a universal tool for the study of neuromuscular disorders, Skelet. Muscle 1 (2011).

[66] F.G. De Angelis, O. Sthandier, B. Berarducci, S. Toso, G. Galluzzi, E. Ricci, G. Cossu, I. Bozzoni, Chimeric snRNA molecules carrying antisense sequences against the splice junctions of exon 51 of the dystrophin pre-mRNA induce exon skipping and restoration of a dystrophin synthesis in Δ48-50 DMD cells, Proc. Natl. Acad. Sci. U. S. A. 99 (2002) 9456–9461.

[67] T. Xu, D. Vavylonis, F.-C. Tsai, G.H. Koenderink, W. Nie, E. Yusuf, I.J. Lee, J.-Q. Wu, X. Huang, SOAX: A software for quantification of 3D biopolymer networks, Sci. Rep.-UK 5 (2015) 9081.

[68] A. Cardona, S. Saalfeld, J. Schindelin, I. Arganda-Carreras, S. Preibisch, M. Longair, P. Tomancak, V. Hartenstein, R.J. Douglas, TrakEM2 software for neural circuit reconstruction, Plos One 7 (6) (2012).